Physical Principles for Scalable Neural Recording

◁Adam H. Marblestone,[1,2] ◁Bradley M. Zamft,[3] Yael G. Maguire,[3,4] Mikhail G. Shapiro,[5] Thaddeus R. Cybulski,[6] Joshua I. Glaser,[6] P. Benjamin Stranges,[3] Reza Kalhor,[3] David A. Dalrymple,[1,7,8] Dongjin Seo,[9] Elad Alon,[9] Michel M. Maharbiz,[9] Jose M. Carmena,[9,13] Jan M. Rabaey,[9] Edward S. Boyden,[▷8,10] George M. Church,[▷1,2,3] and Konrad P. Kording[▷11,12]

◁ Joint first authors ▷ Joint last authors **1** Biophysics Program, Harvard Univ., Boston, MA 02115, USA **2** Wyss Institute for Biologically Inspired Engineering at Harvard Univ., Boston, MA 02115, USA **3** Dept. of Genetics, Harvard Medical School, Boston, MA 02115, USA **4** Plum Labs LLC, Cambridge, MA 02142, USA **5** Division of Chemistry and Chemical Engineering, California Institute of Technology, Pasadena, CA 91125, USA **6** Interdepartmental Neuroscience Program, Northwestern Univ., Chicago, IL 60611, USA **7** Nemaload, San Francisco, CA 94107, USA **8** Media Laboratory, Massachusetts Institute of Technology, Cambridge, MA 02139, USA **9** Dept. of Electrical Engineering and Computer Science, Univ. of California at Berkeley, Berkeley, CA 94720, USA **10** Depts. of Brain and Cognitive Sciences & of Biological Engineering, Massachusetts Institute of Technology, Cambridge, MA 02139, USA **11** Depts. of Physical Medicine and Rehabilitation & of Physiology, Northwestern Univ. Feinberg School of Medicine, Chicago, IL 60611, USA **12** Sensory Motor Performance Program, The Rehabilitation Institute of Chicago, Chicago, IL 60611, USA **13** Helen Wills Neuroscience Institute, Univ. of California at Berkeley, Berkeley, CA 94720, USA

Correspondence to: `adam.h.marblestone` (at) `gmail.com`

(Draft produced July 2, 2013)

> “To understand in depth what is going on in a brain, we need tools that can fit inside or between neurons and transmit reports of neural events to receivers outside. We need observing instruments that are local, nondestructive and noninvasive, with rapid response, high band-width and high spatial resolution… There is no law of physics that declares such an observational tool to be impossible.”
>
> Freeman Dyson, *Imagined Worlds*, 1997

Abstract

Simultaneously measuring the activities of all neurons in a mammalian brain at millisecond resolution is a challenge beyond the limits of existing techniques in neuroscience. Entirely new approaches may be required, motivating an analysis of the fundamental physical constraints on the problem. We outline the physical principles governing brain activity mapping using optical, electrical, magnetic resonance, and molecular modalities of neural recording. Focusing on the mouse brain, we analyze the scalability of each method, concentrating on the limitations imposed by spatiotemporal resolution, energy dissipation, and volume displacement. Based on this analysis, all existing approaches require orders of magnitude improvement in key parameters. Electrical recording is limited by the low multiplexing capacity of electrodes and their lack of intrinsic spatial resolution, optical methods are constrained by the scattering of visible light in brain tissue, magnetic resonance is hindered by the diffusion and relaxation timescales of water protons, and the implementation of molecular recording is complicated by the stochastic kinetics of enzymes. Understanding the physical limits of brain activity mapping may provide insight into opportunities for novel solutions. For example, unconventional methods for delivering electrodes may enable unprecedented numbers of recording sites, embedded optical devices could allow optical detectors to be placed within a few scattering lengths of the measured neurons, and new classes of molecularly engineered sensors might obviate cumbersome hardware architectures. We also study the physics of powering and communicating with microscale devices embedded in brain tissue and find that, while radio-frequency electromagnetic data transmission suffers from a severe power–bandwidth tradeoff, communication via infrared light or ultrasound may allow high data rates due to the possibility of spatial multiplexing. The use of embedded local recording and wireless data transmission would only be viable, however, given major improvements to the power efficiency of microelectronic devices.

1 Introduction

Progress in neuroscience depends on recording the electrical activities of neurons within functioning brains [1]. The classical technique of electrical recording with wired electrodes has made remarkable progress: the number of simultaneously recorded neurons has doubled every seven years since the 1950s, currently allowing electrical observation of hundreds of neurons at millisecond timescales [2].

Recording techniques have recently diversified beyond their roots in electrical recording. For example, activity-dependent optical signals from neurons endowed with fluorescent indicators can be measured by photodetectors, and radio-frequency emissions from excited nuclear spins allow the construction of magnetic resonance images modulated by activity-dependent contrast mechanisms. Other methods have been proposed, including direct recording of neural activities into information-bearing biopolymers [3–5].

Each modality of neural recording has characteristic advantages and disadvantages. Multi-electrode arrays enable the recording of ∼250 neurons at sub-millisecond temporal resolutions. Optical microscopy can currently record ∼100 000 neurons at a 1.25 s timescale in behaving larval zebrafish [6] using light-sheet illumination, or hundreds to thousands of neurons at a ∼100 ms timescale in behaving mice [7] using a 1-photon fiber scope. Magnetic resonance imaging (MRI) allows non-invasive whole brain recordings at a 1 s timescale in humans, but is far from single neuron spatial resolution. Molecular recording devices have been proposed for scalable physiological signal recording but have not yet been demonstrated in neurons [3–5].

Figure 1 illustrates the recording modalities studied here. While further development of these methods promises to be a crucial driver for future neuroscience research, their fundamental scaling limits are not immediately obvious.

Figure 1. Four generalized neural recording modalities. (a) *Extracellular electrical recording* probes the voltage due to nearby neurons. (b) *Optical microscopy* detects light emission from activity-dependent indicators. In two-photon laser scanning microscopy, shown here, an excitation beam at 2x the peak excitation wavelength of the fluorescent indicator is scanned across the sample, while an integrating detector captures the emitted fluorescence. (c) *Magnetic resonance imaging* detects radio-frequency magnetic induction signals from proton spins in water, after weak thermal alignment by a static magnetic field. A resonant radio-frequency pulse tips the spins into a plane perpendicular to the static field, causing the net magnetization to precess. (d) *Molecular recording* devices have been proposed, in which a "ticker-tape" record of neural activity is encoded in the monomer sequence of a biomolecular polymer – a form of nano-scale local data storage. This could be achieved by coupling correlates of neural activity to the nucleotide misincorporation probabilities of a DNA or RNA polymerase as it replicates or transcribes a known DNA strand.

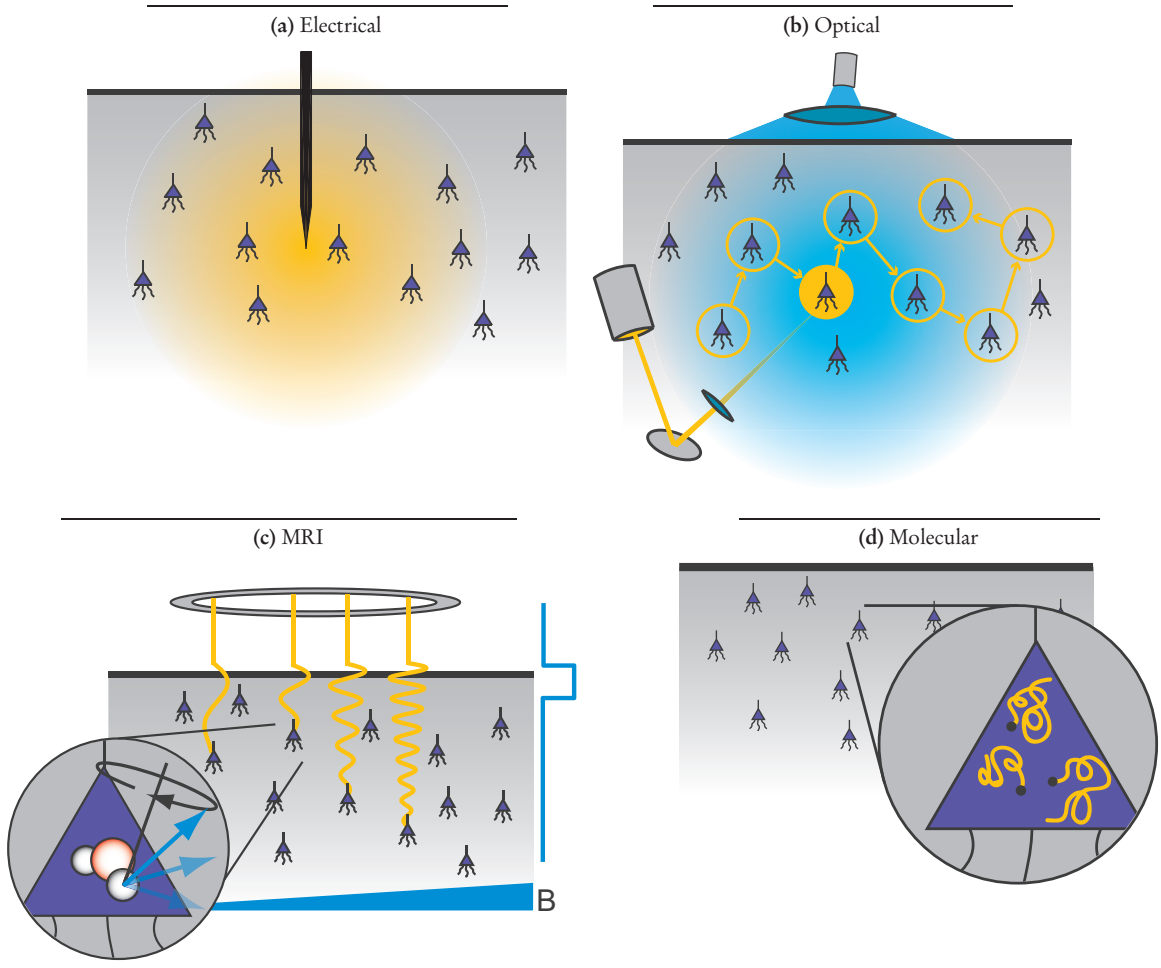

Our analysis is predicated on assumptions that enable us to estimate scaling limits. These include assumptions about basic properties of the brain, which are treated in section 2 (Basic Constraints), as well as those pertaining to the required measurement resolution and the limits to which a neural recording method may perturb brain tissue, which are treated in section 3 (Challenges for Brain Activity Mapping). Together, these considerations form the basis for our estimates of the prospects for scaling of neural recording technologies. We analyze four modalities of brain activity mapping — electrical, optical, magnetic resonance and molecular — in light of these assumptions, and conclude with discussion on opportunities for new developments.

Importantly, our assumptions, analyses and the conclusions thereof are intended as *first approximations and are subject to debate*. We anticipate that as much can be learned from where our logic breaks down as from where it succeeds, and from methods to work around the limits imposed by our assumptions.

2 Basic Constraints

Mouse brain The mouse brain contains $\sim 7.5 \times 10^7$ neurons in a volume of $\sim 420\,\mathrm{mm}^3$ [8] and weighs about 0.5 g. For comparison, the human brain has roughly 8×10^{10} neurons [9] in a volume of $1200\,\mathrm{cm}^3$ [10]. The human brain consumes ∼15 W of power (performing, at synapses, a rough equivalent of at least 10^{17} floating point computational operations per second on that power budget, according to one definition [11], if one insists on making a comparison to a digital computer). Because power consumption scales approximately linearly with the number of neurons [12], the mouse brain is expected to utilize ∼15 mW (for comparison, the metabolic rate of the ∼20–30 g mouse is ∼200–600 mW depending on its degree of physical activity [13]).

Neural activities Action potentials (spikes) last ∼2 ms. The average rate of neuronal spiking is ∼5 Hz [11], but some neurons spike at 500 Hz or faster [14]. The activities of neurons can be highly correlated locally or across large networks [15]. Measuring spike timing with millisecond precision is relevant for understanding network function [16, 17].

Absorption and scattering of radiation All existing methods of neural recording utilize electromagnetic waves, from the near-DC frequencies of wired electrical recordings (∼1 kHz) to the radio-frequencies of wireless electronics and fMRI (MHz–GHz) to visible light in optical approaches (∼500 THz). Electromagnetic waves are attenuated in brain tissue by absorption and scattering. As an approximation to the electromagnetic absorption of brain tissue, we treat the absorption by water, the brain's main constituent (68–80 % by mass in humans [18, 19]). At visible and near-IR wavelengths, there is far worse scattering than absorption: absorption lengths are in the ∼1 mm range, while scattering lengths are ∼25–200 μm [20]. The combined effect of absorption and scattering is measured by the attenuation length, the distance over which the signal strength is reduced by $1/e$ along a path. Figure 2 shows the absorption length of water [21], and the attenuation length in a Mie scattering model (from [22]) intended to approximate the scattering properties of cortical tissue (and see [23] for tissue skin depth measurements in the 10 Hz to 100 GHz range). This gives a preliminary indication of which wavelengths can be used to measure deep-brain signals with external detectors. Note that the attenuation length is only one of several relevant metrics. Importantly, scattering not only causes signal attenuation, but also causes noise and impairs signal separation, so the magnitude of the scattering is a key figure of merit.

Figure 2. Penetration depth (attenuation length) of electromagnetic radiation in water vs. wavelength (data from [24]). Black dashed line: the approximate diameter of the mouse brain. Inset: approximate tissue model based on Mie scattering theory and water absorption. Absorption length of water [21] (blue), tissue scattering length in a simple Mie scattering model (red) and the attenuation length (green) of infrared light calculated based on these approximations (inset reproduced from [21], with permission).

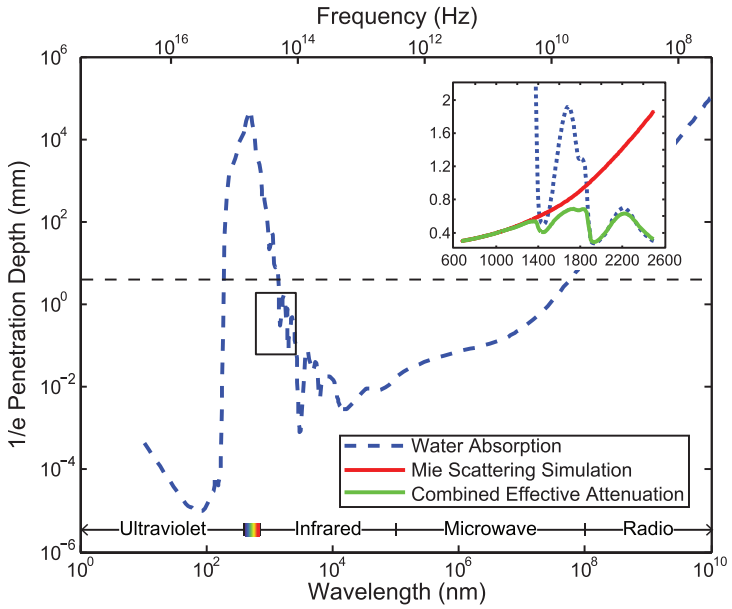

3 Challenges for Brain Activity Mapping

Any activity mapping technology must ideally extract the required information without disrupting normal neuronal activity. As such, we consider three primary challenges:

3.1 Spatiotemporal Resolution

A sampling rate of 1 kHz is necessary to capture the fastest trains of action potentials at single-spike resolution. A minimal data rate of 7.5×10^{10} bits processed per second is then required to record 1 bit per mouse neuron at 1 kHz.

In electrical recording, higher sampling rates (e.g. 10–40 kHz) are often necessary to distinguish neurons based on spike shapes when each electrode monitors multiple neurons. More fundamentally, one bit per neuron sampling at 1 kHz would likely not be sufficient to reliably distinguish spikes above noise: transmitting ~10 bit samples at ~10 kHz (full waveform) or ~10–20 bit time-stamps upon spike detection would be more realistic. On the other hand, it may be possible to locally compress measurements of a spike train before transmission. The degree of compressibility of neural activity data is related to the variability in the distribution of neural responses (e.g., such a distribution may be defined across time bins or repeated stimulus presentations) [25]. In the blowfly Calliphore vicina, the entropy of spike trains has been measured to be up to ~180 bit/s, and the information about a stimulus encoded by a spike train was as high as ~90 bit/s [25]. Extrapolating from fly to mouse, this would suggest that in the worst case, a compression factor of 5×–10× should be possible, relative to a 1000 bit/s raw binary sampling. As a naïve estimate of the entropy as a function of firing rate, one can write the entropy H in bit/s, assuming 1 ms long spikes and 1000 Hz sampling rate, as

$$H \approx \left(-P_{\text{spike}} \cdot \log_2\left(P_{\text{spike}}\right) - \left(1 - P_{\text{spike}}\right) \cdot \log_2\left(1 - P_{\text{spike}}\right)\right) \cdot 1000\,\text{bit/s}$$

where P_{spike} is the probability of spiking during the sampling interval. For the average firing rate of 5 Hz, $P_{\text{spike}} = 0.005$ and $H = 45\,\text{bit/s}$, corresponding to a compression factor of ~20×. However, at 500 Hz, $P_{\text{spike}} = 0.5$ with $H \approx 1000\,\text{bit/s}$, i.e., no compressibility. Therefore, compression could conceivably reduce the data transmission burden for activity mapping by 1–2 orders of magnitude, depending on the neurons and activity regimes under consideration. Based on the above, we assume 1 bit/neuron/ms or 100 Gbit/s for the entire mouse brain, as a "minimal whole brain data rate" in what follows. In many cases, this constitutes a lower bound on what will be feasible in practice.

3.2 Energy Dissipation

Brain tissue can sustain local temperature increases (ΔT) of ~2 °C without severe damage over a timescale of hours and, in rats, changes of this magnitude may occur naturally in response to varying activity levels [26]. Assuming that the brain is receiving a constant power influx $P_{\text{delivered}}$ and that the local thermal transport properties of mouse brains are similar to those of humans, we can approximate the temperature change in deep-brain tissue as a function of the applied power [27, 28]:

$$\frac{\mathrm{d}T}{\mathrm{d}t} = \left(P_{\text{delivered}} + P_{\text{metabolic}} - \rho_{\text{blood}} C_{\text{blood}} f_{\text{blood}} \Delta T\right) \Big/ C_{\text{tissue}}$$

where $P_{\text{metabolic}} = 0.0116\,\text{W/g}$ is the power per unit mass of basal metabolism, $C_{\text{tissue}} \approx 3.7\,\text{J/(K g)} \approx 0.88 \cdot C_{\text{water}}$ is the specific heat capacity of brain tissue, $\rho_{\text{blood}} = 1.05\,\text{g/cm}^3$ is the density of blood, $C_{\text{blood}} = 3.9\,\text{J/(K g)}$ is the specific heat capacity of blood, $f_{\text{blood}} = 9.3 \times 10^{-9}\,\text{m}^3/(\text{g s})$ is the volume flow rate of blood, and ΔT is the temperature difference between the brain tissue and the blood (at temperature 37 °C). A steady-state temperature increase ($\mathrm{d}T/\mathrm{d}t = 0$) of 2 °C corresponds to a power dissipation of ~40 mW per 500 mg mouse brain. Therefore, a recording technique should not dissipate more than ~40 mW of power in a mouse brain at steady state.

Higher power levels may be introduced transiently. According to the above equation, if a neural recorder dissipates ~40 mW per 500 mg mouse brain, then the brain approaches the steady-state temperature in 2–3 min, so shorter experiments may be feasible. Increasing convective heat loss from the brain by increasing blood flow (e.g. via increased heart rate) or cooling [29] the brain, the blood, the cerebrospinal fluid (CSF), or the whole animal, could increase the allowable power dissipation. Note that radiative loss of heat from the brain was ignored here since infrared light emitted by deep-brain tissue is quickly re-absorbed by nearby tissue. We have also assumed that conductive heat loss is negligible at the whole-brain scale compared to the heat extracted by blood flow.

There are also limits on the power density of radiation applied to brain tissue. For radio-frequency electromagnetic radiation, the specific absorption rate (SAR) limit on the power density exposed to human tissue (calibrated for ~1 °C temperature change) is

$\sim$10 mW/cm^2, while for ultrasound (which couples less strongly to dissipative loss mechanisms in tissue) the SAR limit is up to 72× higher. The power density limit for visible and near-IR light exposures are also in the $\sim$10–100 mW/cm^2 range for $\sim$1 ms long exposures, decreasing as the exposure time lengthens (based on the IEC 60825 formulas [30]).

High local power dissipation (transient or steady-state) can also modify the electrical properties of excitable membranes, altering neuronal activity patterns. For example, heating of cell membranes and surrounding solution by millisecond optical pulses leads to changes in membrane electrical capacitance mediated by the ionic double layer [31]. Slower temperature changes (on a scale of seconds) resulting from RF radiation lead to accelerated ion channel and transporter kinetics [32]. Both of these effects are appreciable when the temperature changes are on the order of 1–10 °C.

The above calculations are rough estimates, and further work (e.g., a whole-head simulation [28]) is needed to define the limits of volumetric heat production by neural recording systems distributed throughout the mouse brain. For comparison, common guidelines for biomedical implants [26] use upper limits of 2 °C temperature change, 40 mW/cm^2 heat flux from the surface of implanted brain machine interface (BMI) hardware, and an SAR limit of

$$\frac{\sigma E^2}{2\rho} < 1.6\,\mathrm{mW/g}$$

for electromagnetic energy absorbed by tissue, where E is the peak electric field amplitude of the applied radiation, $\sigma \approx 0.18$ S/m is the electrical conductivity of grey matter and $\rho \approx 1$ g/cm^3 is the tissue density [28] (corresponding to an irradiance of $\frac{\epsilon_0 c}{2} E^2 \approx 2.4$ mW/cm^2). A 96-channel BMI system has been demonstrated in living brains [33] with dissipated areal power density approaching 40 mW/cm^2.

3.3 Sensitivity to Volume Displacement

To prevent damage to the brain, we assume that a recording technique should not cause a brain volume change of > 1 %. The appropriate damage threshold is not yet established, however, so this constitutes a first guess. One important consideration in this regard would be the disruption of blood circulation by inserted material; a high density of implanted material in a brain region could cause stroke due to widespread vascular damage. Recent studies [34] have defined in microscopic detail the complete vascular network of the mouse cortex using high-throughput histology; this type of information could be used to enumerate key vascular pathways which could be spared from damage.

It is possible to insert large numbers of probes throughout multiple brain areas without compromising function. In rats [35], 96 electrodes of 50 μm diameter were simultaneously inserted across four forebrain structures (cortex, thalamus, hippocampus and putamen). In rhesus macaque [36], 704 electrodes of diameter 50 μm and average depth 2.5 mm were chronically implanted in cortex. Note, however, that the total volume displacement in these experiments was below 0.1 %, and below 0.01 %, respectively.

The nature of the volume displacement is important — sheets of instrumentation that sever long-range connectivity, for example, would disrupt normal brain function regardless of the degree of volume displacement. Conversely, higher volume displacement might be possible if introduced gradually, or during early development, insomuch as the brain can adapt without disrupting natural computation.

4 Evaluation of Modalities

We next evaluate neural recording technologies with respect to the above challenges, using the mouse brain as a model system. Table 1 lists the modalities studied, the assumptions made, the analysis strategies applied, and the conclusions derived.

4.1 Electrical Recording

In the oldest strategy for neural recording, an electrode is used to measure the local voltage at a recording site, which conveys information about the spiking activity of one or more nearby neurons. The number of recording sites may be smaller than the number of neurons recorded since each recording site may detect signals from multiple neurons. Traditional electrical recording techniques keep active devices such as amplifiers outside the skull and therefore do not pose a heat dissipation challenge; this may change if amplifiers are brought closer to the signal sources to reduce noise.

Table 1: Summary of modalities, models, assumptions and conclusions

Modality	Analysis Strategy	Assumptions	Conclusions
Extracellular electrical recording	Compute minimal number recorders based on max distance from recorder to recorded neuron	Decay profile of extracellular voltage Approximate noise levels at recording site	Maximum recording distance $r_{max} \approx 100$–$200\,\mu$m from electrode to neuron measured $\sim 100\,000$ recording sites are required per mouse brain at current noise levels However, $\sim 10^7$ electrodes are required in practice to enable sorting of noisy, temporally overlapping spikes using current algorithms
Implanted electrical recorders	Compute power dissipation of electronic devices that digitally sample neuronal activity	Physical limit: $k_B T \ln(2)$/ bit erased Practical limit: $\sim 10 k_B T$/ bit processed Current CMOS digital circuits: $> 10^5 k_B T$/ bit processed	Requires at least 2–3 orders of magnitude increase in the power efficiency of electronics relative to current devices to scale to whole-brain simultaneous recordings Minimalist architectures should be developed to reduce local data processing overhead
Wireless data transmission	Compute tradeoff between power efficiency and channel bandwidth using information theory	Transmitter must supply enough power to overcome noise and path loss	Data transmission at optical or near-optical frequencies is necessary to achieve sufficient single-channel data rates using electromagnetic radiation. Radio-frequency (RF) electromagnetic transmission of whole-brain data would draw excessive power due to bandwidth constraints. Bandwidth cannot effectively be split over multiple independent RF channels, but IR light or ultrasound may allow spatial multiplexing.
Optical imaging	Relate the scattering and absorption lengths of optical wavelengths in brain tissue to signal-to-noise ratios for optical imaging	Approximate values of scattering and absorption lengths as a function of wavelength	Light scattering imposes severe limits on optical techniques, but strategies exist which could negate the effects of scattering, such as implantable optics, infrared fluorescence or bioluminescence, and online inversion of the scattering matrix
Multi-photon optics	Compute minimum total excitation light power to excite multi-photon transitions from indicators within each neuron in every imaging frame	Approximate values of multi-photon cross-sections Pulse durations similar to those currently used in multi-photon imaging	Multi-photon pulsed-laser excitation of a whole mouse brain will over-heat the brain except in very short experiments
Beam scanning microscopies	Calculate device and indicator parameters necessary for fast beam re-positioning and signal detection	Fast optical phase modulators could re-position beams at ~ 1 GHz switching rates Fluorescence lifetimes in the 0.1–1.0 ns range	Beam re-positioning time limits the speed of current systems but we are far from the physical limits of scan speed Fluorescence lifetimes of indicators may constrain design of ultra-fast scanning microscopies
Magnetic resonance imaging	Calculate spatial and temporal resolution of MRI based on spin relaxation times and spin diffusion	Proton MRI using tissue water Approximate values of T_1 and T_2 relaxation times and self-diffusion times for tissue water	To a first approximation, proton MRI is limited by the T_1 relaxation time of water to ~ 100 ms temporal resolution and by the self-diffusion of water to spatial resolutions of $\sim 40\,\mu$m. T_1 pre-mapping could allow T_2 contrast on a ~ 10 ms timescale.
Ultrasound	Calculate spatial resolution, signal strength and bandwidth limits on ultrasound imaging	Speed of sound in brain Attenuation rate of ultrasound in brain	Attenuation of ultrasound by brain tissue and bone may be prohibitive at the ~ 100 MHz frequencies needed for single-cell resolution ultrasound imaging Ultrasound may be a viable medium for spatially multiplexed data transmission from embedded devices
Molecular recording	Compute metabolic load and DNA volume for rapid synthesis of large nucleic acid polymers Evaluate temporal resolution in simulated experiments using kinetic models	Polymerase biochemical parameter ranges Metabolic requirements of genome replication	Molecular recording devices fall within physical limits but their development poses major challenges in synthetic biology

4.1.1 Spatiotemporal Resolution

One way to estimate the minimal number of electrodes required to record from the entire mouse brain is to extrapolate the state of the art in spike sorting. In an optimistic scenario, ~10 neurons per electrode may be distinguishable using current spike-sorting algorithms [37–39], although the theoretical upper bound is unknown. Indeed, most current techniques (e.g. hand-positioned tetrodes) optimize for signal separability, not for total number of recorded neurons. This scenario would necessitate $N = 7.5 \times 10^6$ electrodes to record from all mouse neurons. This could correspond to recording sites spaced on the vertices of a $\sim 200 \times 200 \times 200$ site cubic lattice with ~40 μm edge length.

A more optimistic estimate, neglecting difficulties with spike sorting, derives from the maximum distance between an extracellular electrical recorder and a neuron from which it records spikes. In a first approximation, this is determined by two factors: the decay of the signal with distance from the spiking neuron and the background noise level at the recording site. We assume that for an electrode to reliably detect the signal from a given neuron, the magnitude of that neuron's signal must be larger than the electrode's noise level. Note, however, that knowledge of spike shape distributions could potentially be used to extract low-amplitude spikes from noise.

The peak signals of spikes from neurons immediately adjacent to an electrode are in the 0.1–1.0 mV range and scale roughly as e^{-r/r_0}, where r is the distance from the cell surface and the $1/e$ falloff distance r_0 has been experimentally measured at ~28 μm in both salamander retina [40] and cat cortex [41], and computed at ~18 μm in a biophysically realistic simulation [42]. However, this decay is strongly influenced by the detailed geometry of neuronal currents and the properties of the extracellular space, making analytical calculation of the decay rate difficult (at large distances, a much slower $1/r^2$ dipole falloff is expected).

Several sources of background noise enter the recordings. Johnson noise, which arises from thermal fluctuations in the electrode, is

$$V_{\text{johnson}} = \left(4 k_B T Z \text{BW}\right)^{1/2}$$

which for physiological temperature, electrodes of impedance $Z = 0.5\,\text{M}\Omega$, and $\text{BW} = 10\,\text{kHz}$ bandwidth is $V_{\text{johnson}} \approx 9\,\mu\text{V}$. The recordings are also affected by interference from other neurons, which has been reported to exceed the Johnson noise, and is non-stationary due to changes in the cells' firing properties [38]. The noise and interference from these sources realistically produces > 10–20 μV of voltage fluctuations [39]. Current recording setups thus have signal to interference-plus-noise ratios (SINRs) of < 100, where the SINR is defined as the ratio of the peak voltage from immediately adjacent neurons to the voltage fluctuation floor of the electrode.

A limit on the maximum recording distance is the distance at which the signal from the farthest neuron falls below the noise floor, $r_{\text{max}} \approx r_0 \ln(\text{SINR})$. For $\text{SINR} \approx 100$, $r_{\text{max}} \approx 130\,\mu\text{m}$. For comparison, recent experimental data from multi-site silicon probes has shown few detectable neurons beyond ~100 μm and none detectable beyond 160 μm [43]. Recordings in the hippocampal CA1 region could not detect spikes from cells farther than 140 μm from the electrode tip [44], even after averaging over observations triggered on an intracellularly recorded spike; in hippocampus, this corresponds to a detection volume containing approximately 1000 neurons [45]. Furthermore, in many studies (in monkeys, rats and mice) using multi-electrode arrays with 150–300 μm inter-electrode spacings, no neuron is seen by more than one electrode [46–49].

Due to the steep local falloff, even improving the SINR by a factor of 10 only extends the maximal recording distance to $r_{\text{max}} \approx 190\,\mu\text{m}$. Assuming packing of the brain into equal sized cubes of side length $d = \sqrt{2} r_{\text{max}} \approx 180\,\mu\text{m}$ gives $N > 69000$ electrodes for whole brain recording using recording sites with $r_{\text{max}} \approx 130\,\mu\text{m}$. Note that N varies as the third power of r_{max} and is therefore highly sensitive to variations in the assumed maximal recording distance; the number of required recorders can range from 21000 to 110000 as r_{max} varies from 190 μm to 110 μm.

Importantly, this calculation underestimates the required number of electrodes in practice, because sorting spikes from all neurons within the $6 \times 10^6\ \mu\text{m}^3$ cube corresponding to a single electrode is likely to be unrealistic for several reasons. First, signals from the weakest cells are far weaker than those from the strongest cells and the signals from some cells decay much faster than others [41]. Second, because of neuronal synchronization, the local noise produced by nearby neurons may sometimes be large. Finally, with many neurons per electrode or at high firing rates, spikes from detectable neurons will often temporally overlap, making spike sorting difficult. This would be exacerbated by correlated firing patterns of nearby neurons.

4.1.2 Volume Displacement

We require < 1 % total volume displacement from N recorders. Wires from each electrode must make it to the surface of the brain, which implies an average length $\ell \approx 4\,\text{mm}$ for the mouse brain (depending on assumptions about the wiring geometry).

As a rough approximation we consider each recorder to produce a volume displacement associated with a single cylindrical wire, with length ℓ and radius r. Thus r must satisfy

$$\pi r^2 \ell N_{\text{min,rd}} < 0.01 V_{\text{brain}}$$

Using $N_{\mathrm{min,rd}} = 110000$ or 21000 recording sites and $\ell \approx 4\,\mathrm{mm}$ requires wires of radius $r_{\mathrm{max}} \approx 8.0\,\mu\mathrm{m}$, or $3.4\,\mu\mathrm{m}$, respectively. While these dimensions are readily achievable using lithographic micro-fabrication, there would be a challenge to produce *isolated* wires of such dimensions at scale (perhaps suggesting the use of wire bundles). Still, the volume constraints are unlikely to limit whole-mouse-brain electrical recording even in the most pessimistic scenario.

Figure 3 illustrates the above considerations as a function of the electrode SINR.

Figure 3. The voltage signal to interference-plus-noise ratio (SINR) at the recording site sets an approximate upper bound on the distance r_{max} between the recording site and the farthest neuron it can sense (blue). Assuming at least one electrode per cube of edge length $\sqrt{2}r_{\mathrm{max}}$ in the mouse brain in turn limits the number of neurons per recording site (gold), the total number of recording sites (red) and the diameter of wiring consistent with $< 1\,\%$ total brain volume displacement (turquoise). SINR values for current recording setups are $< 10^2$. In practice, the number of neurons per electrode distinguishable by spike-sorting algorithms is only $\sim$10, so these curves greatly under-estimate the number of electrodes which would be required based on current spike-sorting approaches.

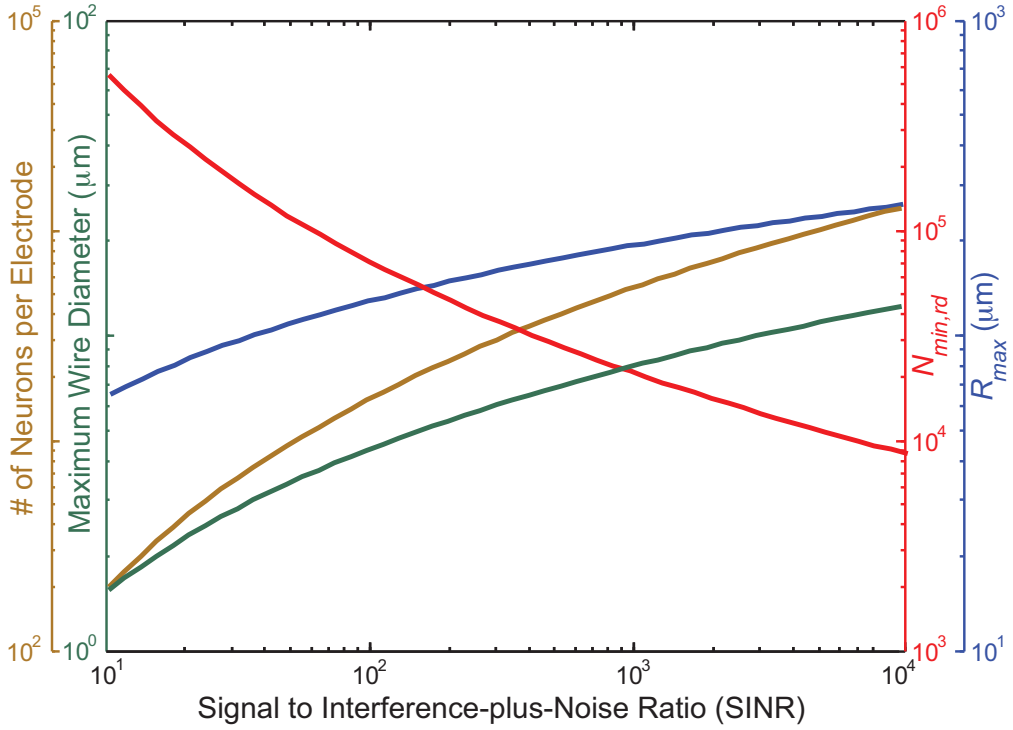

4.1.3 Implanting Electrodes in the Brain

There are several technology options for introducing many electrodes into a brain. For example, flexible nanowire electrodes could, in theory, be threaded through the capillary network [50]. Capillaries are present in the brain at a density of 2500–3000 per mm^3 [51], which equates to one capillary per 73 μm, with each neuron lying within ∼200 μm of a capillary [52]. The cerebrospinal ventricles may also provide a convenient location for recording hardware. Neural tissues could be grown around pre-fabricated electrode arrays [53], or silicon probes arrays with many nano-fabricated recording sites per probe [43] could be inserted into the brain.

Mechanical forces during insertion and retraction of silicon and tungsten microelectrodes from brain tissue have been measured in rat cortex at ∼1 mN for electrodes of ∼25 μm radius [54]. These forces are comparable to the Euler bucking force F of a 2 mm long cylindrical tungsten rod of 5 μm radius

$$F = \frac{\pi^2 EI}{(KL)^2} \approx 1\,\mathrm{mN}$$

where $E = 411\,\mathrm{GPa}$ is the elastic modulus of tungsten, $I = (\pi/2)(5\,\mu\mathrm{m})^4$ is the area moment of inertia of the cylindrical wire cross-section, $L \approx 2\,\mathrm{mm}$ is the length of the wire, and K is the column effective length factor which depends on the boundary conditions and is set to $K = 1$ here for simplicity. This suggests that it may be possible to push structures of $< 10\,\mu\mathrm{m}$ diameter into brain tissue (see [55] for related calculations). It might be advantageous to pull rather than push wires into the brain (e.g., using applied fields, or cellular oxen [56] to carry the wires), since the thinnest wires could withstand tension forces much higher than the compressive force at which they buckle (although there may be ways to circumvent buckling, e.g., via rapid vibration).

4.1.4 Conclusions and Future Directions

Electrical recording has the advantage of high temporal resolution, but the large number of required recording sites poses challenges for delivery mechanisms. Ongoing innovations which could enable viable all-electrical recording methods include the development of highly multiplexed probes, thinner wires, smaller electrode impedances, amplifiers with lower input-referred noise levels, novel methods to implant large numbers of electrodes, multilayer lithography for routing electrical traces, spike sorting algorithms capable of handling temporally overlapping, non-independent spikes and adaptively modeling the noise, and hybrid systems integrating electrical recording with implantable optics or other methods.

A caveat, however, pertains to the ability to relate the measured electrical signals to specific cells within a circuit. As the set of neurons recorded by each electrode grows to encompass a large volume around the electrode, it will become more difficult to attribute the recorded spikes to particular neurons. Furthermore, given the complex geometries of neuronal processes, it is not obvious how to determine the spatial position or layout of a neuron from its electrical signature on a nearby electrode. A given electrode will be positioned near the axons or dendrites of some neurons, and near the cell bodies of other neurons, complicating data interpretation. If the spatial density of recording sites is increased such that many electrodes sample the same neuron, however, this could enable imaging of neuronal morphology via voltage signals across multiple electrodes. Currently, extracellular recording also does not allow extraction of molecular information on the cells being recorded, although intracellular electrophysiological recording methods (e.g., automated patch clamp [57]) might enable this for a limited number of cells.

4.2 Optical Recording

Optical techniques measure activity-dependent light emissions from neurons, generated by fluorescent indicator proteins (although activity-dependent bioluminescent emissions are an emerging possibility). Calcium indicators can only distinguish spikes below ∼50–100 Hz firing rates without averaging [58], but the field of high-speed fluorescent voltage indicators is advancing quickly [59–61].

4.2.1 Spatiotemporal Resolution

Multiplexing strategies The signal from each neuron must be separated from emissions originating at other points in the brain. Epi-fluorescence microscopy images a plane in the specimen onto a spatially-resolved two-dimensional detector (e.g., a CCD camera), while all neurons in a 3D volume are illuminated. The focal plane is scanned through the sample to achieve 3D coverage. Out-of-focus neurons add background noise; light sheet imaging illuminates only neurons near the focal plane, reducing this noise, but requires transparent brains [6]. In multi-photon microscopy, nonlinearities result in fluorescence excitation occurring only near the focal point of the excitation laser, which is scanned across the sample. In confocal scanning microscopy, only photons from a point of interest are measured due to geometric constraints (e.g., pinholes). Optical techniques thus achieve signal separation by multiplexing spatially (e.g., direct imaging) or temporally (e.g., beam scanning), and often by a combination of the two.

Effects of light scattering Single-photon techniques limit imaging to a depth of a few scattering lengths at the excitation and emission wavelengths of activity indicators (up to ∼1–2 mm for certain infrared wavelengths [22, 62, 63] vs. a few hundred μm for visible wavelengths [20]). Activity dependent dyes are currently available only in the visible spectrum; indicators operating in the infrared (see [64–66] for far-red fluorescent proteins) could improve imaging depth.

Multi-photon excitation takes advantage of the deeper penetration of infrared light. Two or more infrared photons may together excite a fluorophore with an excitation peak in the visible range, leading to the emission of a visible photon. If only one neuron is illuminated with sufficient intensity to generate multi-photon excitation, all photons captured by the detector originate from that neuron, regardless of the scattering of the outgoing light. Hence, the emission pathway is limited less by scattering than by absorption. This has resulted in imaging at > 1 mm depth [22, 62, 63].

There are at least four options for overcoming the scattering of visible light to enable signal-separation from deep-brain neurons [1, 67]:

1. Infrared light can excite multi-photon fluorescence in an excitation-scanning architecture.
2. Fluorophores with both excitation and emission wavelengths in the infrared could be developed.
3. Emerging techniques based on beam shaping allow transmission of focused light through random scattering media by inverting the scattering matrix [68]. Because the scattering properties change over time, this must be done quickly, possibly faster than the imaging frame rate, necessitating high-speed wavefront modulation. This can currently be achieved with digital micro-mirror devices (DMDs), but not with phase-only spatial light modulators (SLMs), although GHz switching of phase modulators appears feasible in principle [67]. High speed focusing through turbid media is also achievable using all-optical feedback in a laser cavity [69]. It is possible to measure the scattering matrix non-invasively [70] using a photo-acoustic microscopy based on focused ultrasound.

4. Light sources and/or detectors could be positioned close to the measured neurons, necessitating the use of embedded optical devices. This could be done using optical fiber [71] and/or waveguide [72, 73] technologies, which are developing rapidly. For example, single-mode fiber cables can support > 1 TB/s data rates with low light loss over hundreds of kilometers.

While optics might seem to require a number of photodetectors, fibers or waveguide ports comparable to the number of neurons, new developments suggest ways of imaging with fewer elements. For example, compressive sensing or ghost imaging techniques based on random mask projections [74–77] might allow a smaller number of photodetectors to be used. In an illustrative case, an imaging system may be constructed simply from a single photodetector and a transmissive LCD screen presenting a series of random binary mask patterns [78], where the number of required mask patterns is much smaller than the number of image pixels due to a compressive reconstruction. Furthermore, it is possible to directly image through gradient index of refraction (GRIN) lenses [79] or optical fibers [71, 80, 81], thus multiplexing multiple observed neurons per fiber.

Hybrid techniques combining optics with other modalities may also provide new ways to overcome scattering. For example, ultrasound encoding [82], which frequency-tags light emissions emerging from a known location via a mechanical Doppler shift of the emitter [83], is powerful in that it provides a generic mechanism to sidestep problems of elastic optical scattering, but it requires distinguishing MHz frequency modulations in THz light waves (part per million frequency discrimination).

Speed of beam scanning Multi-photon and confocal approaches rely on the serial scanning of an excitation beam across the sample. The speed of scanning microscopes is limited by beam re-positioning times ($\sim$0.1 µs for spinning disk [71, 80, 81], $\sim$3 µs for piezo-controlled linear scan mirrors, $\sim$10 µs for acousto-optic deflectors [84], $\sim$8 kHz line scans for resonant galvanometer mirrors), and the fluorescence lifetimes of activity indicators ($\sim$1 ns). Note that 0.1 µs repositioning time for current spinning-disk confocal techniques would require 10 seconds per frame for whole mouse brain imaging with a single scanned beam: $\left(10^{-7}\,\text{s/site}\right)\left(10^{8}\,\text{site/brain}\right) = 10\,\text{s/brain}$. There is therefore a need for a 10^4 fold improvement in beam re-positioning time and/or beam parallelization in order to achieve 1 kHz imaging frame rates for whole mouse brains. The 10 µs repositioning time for acousto-optic deflectors is set by the speed of sound in the deflector crystal, while scanning mirrors and spinning disks are limited by inertia. In principle, however, optical phase modulators could switch at GHz rates [67] and arrays of such phase modulators could arbitrarily re-shape coherent optical wavefronts to re-position beamlets. Moreover, parallelization of beamlets and detectors could allow further speedups. The speed of beam scanning is thus far from its physical limits. Fluorescence lifetimes in the 0.1–1 ns range [85] may ultimately constrain the design of scanning microscopies: a delay of 0.1 ns per mouse neuron per frame corresponds to 100 Hz frame rate with no parallelization.

Diffraction Due to diffraction, a lens (or other limiting optical aperture) above a minimum diameter is necessary to achieve a given angular resolution, and it might be hypothesized that this would be limiting factor for optical methods. However, this is not the case. To illustrate, at a depth of 10 mm we must be able to distinguish two neurons which are 10 µm apart. In the small angle approximation, we have $\theta \approx (10\,\mu\text{m})/(10\,\text{mm}) \approx \lambda/D$. Therefore, using light of wavelength $\lambda \approx 1\,\mu$m requires a lens aperture D of only 1 mm. As such, it seems that diffraction is not a significant limiting factor for cellular resolution imaging, at least outside the context of microscale apertures that might find use in embedded optics approaches.

4.2.2 Energy Dissipation

Light that does not leave the brain is ultimately dissipated as heat. The total light power requirements for optical measurement of neuronal activity using fluorescent indicators depend on factors including fluorophore quantum efficiency, absorption cross-section, activity-dependent change in fluorescence, background fluorescence, labeling density, activation kinetics, detector noise, scattering and absorption lengths, and others. Unfortunately, many of these variables are unknown or highly dependent on particular experimental parameters.

A statistical analysis of photon count requirements for spike detection (in the context of calcium imaging) can be found in [86], which derived a relationship between the number of background photon counts (N_{bg}) and the required number of signal photon counts required for high fidelity spike detection given photon shot noise, scaling roughly as $N_{\text{signal}} > 3\sqrt{2N_{\text{bg}}}$, even at low absolute photon count rates. While this analysis governs the number of detected photons, the number of emitted photons will be higher due to losses. In one example using two-photon excitation, 5 % of the emitted photons were captured by the photodetector [87].

Multi-photon: current technology Multi-photon excitation poses a particularly severe power problem due to the high light intensities required to excite nonlinear optical processes. In typical multi-photon experiments on mice, $\sim$50 mW of time-averaged laser power is used with a dwell time of $\sim$3 µs [88]. This would allow imaging $\sim$300 neurons at millisecond resolution with a single scanned excitation beam. Current multi-photon imaging experiments are already near the permissible energy dissipation limit and improvements cannot come at the cost of greatly increased light power delivery.

Multi-photon: theoretical calculations Multi-photon experiments rely on short laser pulses with high peak light intensities at a focused excitation spot to excite nonlinear transitions [87]. This imposes an experimentally relevant physical limit: at least one excitation pulse of sufficient intensity per neuron per frame is required in order to excite multi-photon fluorescence during each frame. Assuming 1 kHz frame rate and 0.1 nJ pulses, delivering only one pulse per neuron per frame would dissipate roughly $\left(10^8\right)\left(1\,\text{kHz}\right)\left(0.1\,\text{nJ}\right) = 10\,\text{W}$ in the mouse brain, which is clearly prohibitive. This is a lower bound because, in general, more than one excitation pulse per neuron per frame may be required to excite detectable fluorescence (e.g., one reference reported 12 pulses per spot [87]). For three-photon excitation, the situation will be even worse as higher peak light intensities are required to excite three-photon fluorescence.

Could the single-pulse energy be reduced while maintaining efficient two-photon excitation? The number of two-photon (2P) transitions excited per fluorophore per pulse is $n_a = F^2 C/t$, where F is the number of photons per pulse per area, in units of photon/cm^2, C is the two-photon cross-section in units of cm^{4}s/photon, and t is the pulse duration in seconds. This can be approximated as

$$n_a = \left(\frac{\frac{E}{hc/\lambda}}{\left(\frac{\lambda}{2(\text{NA})}\right)^2}\right)^2 \frac{C}{t} = \left(\frac{4E\left(\text{NA}\right)^2}{hc\lambda}\right)^2 \frac{C}{t}$$

where NA is the numerical aperture of the focusing optics, E is the pulse energy and λ is the stimulation wavelength. For a 2P experiment with 100 fs, 0.1 nJ pulses, assuming a 2P cross section [89, 90] of 10^{-48} cm^{4}s/photon (i.e., 100 Goeppert-Mayer units [91], comparable to that of DsRed2 [90]), $\lambda = 900$ nm and NA = 1.0, $n_a \approx \frac{1}{2}$. Thus, a few pulses are likely necessary and sufficient to excite 2P fluorescence by each fluorophore within the focal spot. With a 2P cross section approaching 10^{-47} cm^{4}s/photon (1000 Goeppert-Mayer units), one could reduce the pulse energy by an order of magnitude (and hence n_a by two orders of magnitude) while maintaining $n_a > \frac{1}{20}$, i.e., one in twenty fluorophores excited by each pulse. Reducing the pulse energy much further might lead to unacceptably low excitation levels. Alternatively, shorter pulse durations could increase the light intensity, and hence 2P excitation probability, at fixed pulse energy.

4.2.3 Bioluminescence

To work around the requirement for large amounts of excitation light, bioluminescent rather than fluorescent activity indicators could be used. Consider a hypothetical activity-dependent bioluminescent indicator emitting at ~1700 nm (IR), in order to evade light scattering. As a crude estimate, assuming that 100 photons must be collected by the detector per neuron per 1 ms frame, and 1 % light collection efficiency by the detector relative to the emitted photons, ~100 μW of emitted bioluminescent photons emissions are required for the entire mouse brain. This would be feasible from the perspective of heat dissipation. By contrast, in a 1-photon fluorescent scenario, if 100 excitation photons must be delivered into the brain to generate a single fluorescent emission photon, the power requirement becomes 10 mW, which is on the threshold of the steady-state heat dissipation limit. Therefore, bioluminescent indicators could potentially circumvent problems of heat dissipation associated with whole-brain optical imaging even in the 1-photon case.

The widely used bioluminescent protein firefly luciferase is ~80 % efficient in converting ATP hydrolysis coupled with luciferin oxidation into photon production, yielding ~0.8 photons per ATP-luciferin pair consumed [92], and has ~90 % energetic efficiency in converting free energy to light production. Heat dissipation associated with the luciferase biochemistry itself is therefore not a significant overhead relative to the 100 μW of emitted photons calculated above. In the same scenario, however, the brain would consume $\sim 6 \times 10^8$ additional ATP molecules per minute per neuron in order to power the bioluminescence, which is within the limits of cellular aerobic respiration rates (~1 fmol O_2 per minute per cell [93], with ~30 ATP per 6 O_2, hence 3×10^9 molecules ATP synthesized per minute from ADP via glucose oxidation), but not by a large margin. Transient increases in metabolic rate are possible: energy dissipation more than doubles in the mouse during high physical activity [13]. Therefore, whole-brain activity-dependent bioluminescence, at speeds high enough to achieve millisecond frame rates, may be metabolically taxing for the cell but is nevertheless plausible as a light generation strategy. Note that we have not treated the energy required to bio-synthesize the luciferin compound, which may create additional overhead (though conceivably luciferin could be provided exogenously).

4.2.4 Conclusions and Future Directions

Scattering of visible light in the brain creates a problem of signal-separation from deep-brain neurons. Multi-photon techniques, which scan an infrared excitation beam, can work around this scattering problem. However, current multi-photon techniques applied at whole brain scale would dissipate too much power to avoid thermal damage to brain tissue. Systems (such as plasmonic nano-antennas [94]) that could locally excite multi-photon fluorescence without the need for high-energy laser pulses could conceivably

ameliorate this issue. Furthermore, scanning microscopies require orders of magnitude improvement in speed or parallelization to apply to whole brains. This speed improvement may ultimately be limited by fluorescence lifetimes of the indicators. New methods besides multi-photon techniques could also work around the scattering of visible light in the brain. For example, fluorophores or bio-luminescent proteins could be developed which operate at infrared wavelengths. A compelling example from nature is the black dragonfish, which generates far red light (∼705 nm) via a multi-step bioluminescent process (using this light to see in deep ocean waters) [95, 96]. A large set of activity indicators with distinguishable colors, generated through a combinatorial genetic recombination mechanism such as BrainBow [97], could also improve signal separation (e.g., in conjunction with static post-mortem microscopy to map between cell colors and positions). In addition, implanted optical devices, which place emitters and detectors within a few scattering lengths of the neurons being probed, could potentially obviate the negative effects of scattering and allow visible-wavelength indicators to be used without a need for multi-photon excitation.

4.3 Embedded Active Electronics

The preceding sections have assumed that electrical or optical signals from the recorded neurons are shuttled out of the brain before digitization and storage, but it is also conceivable to develop embedded electronic systems that locally digitize and then store or transmit (e.g., wirelessly) measurements of the activities of nearby neurons. This could allow for shorter wires in electrical recording approaches, and for shorter light path lengths in optical recording approaches, as well as for more facile (e.g., non-surgical) delivery mechanisms for the recording hardware.

Integrated circuits have shrunk to a remarkable degree: in about 3 years, following the Moore's law trajectory, it will likely be possible to fit the equivalent of Intel's original 4004 micro-processor in a 10 μm × 10 μm chip area. Functional wirelessly powered radio-frequency identification (RFID) chips as small as 50 μm [98] in diameter have been developed and tags with chip-integrated antennas function at the 400 μm [99] scale. Integrated neural sensors including analog front ends are also scaling to unprecedented form factors: a 250 μm × 450 μm wireless implant – including the antenna, but not including a ∼1 mm electrode shank used to separate signal from ground – draws only 2.5 μW per recording channel [100]. The system operates at ∼1 mm range in air, powered by a transmitter generating ∼50 mW of transmitted power. Note that for a single such embedded recording device, the heat dissipation constraint is set not by the device's own dissipation (10 μW for four recording channels) but rather by the RF specific absorption rate limit associated with the 50 mW transmit power. Remarkably, cells such as macrophages (∼13 μm in size) can engulf structures up to at least 20 μm in diameter [101] and have been studied as potential delivery vehicles for nano-particle drugs [102], suggesting possibilities for non-surgical delivery of embedded electronics to the brain.

If a large amount of local storage is used, the real-time transmission bandwidth requirements for neural recording could be significantly reduced if it is only desired to take a "snapshot" of neural activity patterns over a limited period of time. For example, flash memory, which will likely be the densest form of electronic memory storage in the near future, can store 1 Mbit of data in a device 100 μm on a side. Even denser forms of memory storage are under development and could perhaps be used in a one-time-write mode in the context of neural recording long before they become commercially viable for use as rewritable media in the consumer electronics industry.

Here we consider the power dissipation associated with embedded electronic recording devices, as well as the constraints on possible methods to power them. In the next section, we describe how physics constrains the achievable data transmission rates from such devices.

4.3.1 Power Requirements for Recording

Any embedded system needs to process data, in preparation either for local storage or wireless transmission. Physics defines hard limits on the required power consumption associated with data processing (neglecting the possibility of reversible logic architectures [103]), arising from the entropy cost for erasing a bit of information [104]:

$$E_{\text{Landauer}} = \ln(2)\, k_B T \approx 3 \times 10^{-21}\,\text{J/bit} \qquad \text{(the Landauer limit)}$$

Ambitious yet physically realistic values for beyond-CMOS logic lie in the tens of $k_B T$ per bit processed [105]. Scaling $40\, k_B T$/bit to record raw voltage waveforms at a minimal 1 kbit/s/neuron (e.g. 1 kHz sampling rate, 1 bit processed per neuron per sample), the total power consumption for whole mouse brain recording could in principle be as low as ∼16 nW. Thus, at the physical limits of power efficiency, implanted devices could in principle digitally buffer and locally store a complete record of a mammalian brain's activity. While this leaves $> 10^6$-fold room for overhead due to increased data processing burden (more required bit flips per second), or energetic inefficiency of the switching device (greater dissipation per bit), realistic devices in the near-term may in fact require this much overhead, if not more. This necessitates a more detailed consideration of limiting factors for today's microelectronic devices.

In the context of electrical recording, the first step that must be performed by an embedded neural recording device is digitization of the voltage waveform. Until mV-scale switching devices are developed (see discussion below), it is necessary to amplify the ∼10–100 μV spike potential in order to drive digital switching events in downstream gates. During this sub-threshold amplification step, a CMOS (or BJT) device will dissipate static power (associated with a bias current). Importantly, in order to decrease the input-referred voltage noise of this amplification process, it is necessary to increase the bias current and hence the static power dissipation. For a simple differential transistor amplifier, the minimal bias current scales as

$$I_{\mathrm{d}} = \frac{\pi}{2}\frac{4k_{\mathrm{B}}T}{V_{\mathrm{n,max}}^2}\frac{k_{\mathrm{B}}T}{q}\mathrm{BW}$$

where $V_{\mathrm{n,max}}$ is the input-referred voltage noise of the amplifier and q is the electron charge. For an extracellular recording with $\mathrm{BW} = 10\,\mathrm{kHz}$ and $V_{\mathrm{n,max}} = 10\,\mu\mathrm{V}$, this implies a minimal bias current $I_{\mathrm{d}} \approx 60\,\mathrm{nA}$ or a minimal static power of $(I_{\mathrm{d}} V_{\mathrm{dd}}) \approx 6 \times 10^{-8}\,\mathrm{W}$ at $V_{\mathrm{dd}} \approx 1\,\mathrm{V}$ operating voltage. Assuming 10 neurons per recording channel, we then have 7.5 million recording channels for a mouse brain, which gives a power dissipation associated with signal amplification of ∼500 mW. Note that realistic analog front ends (which are subject to $1/f$ noise and require multiple gain stages) draw 6×–10× greater bias current, quantified by the noise efficiency factor (NEF) [106], to achieve the same input-referred noise levels.

Local on-chip digital computation also incurs an energy cost. Current CMOS digital circuits consume 5–6 orders of magnitude [105, 107–109] more energy per switching event (∼1 fJ/bit including charging of the wires [107]) compared to the Landauer limit (e.g., for a digital CMOS inverter, and ignoring the static power associated with the leakage current). This corresponds to a ∼1 fF total load capacitance at 1 V operating voltage. For 100 GHz switching rates (10^8 neurons × 1 kHz) as above, this corresponds to 0.01–0.1 mW. Realistic architectures, however, will incur overhead in the number of switching events required to store, compress and/or transmit neural signals, likely bringing the power consumption into an unacceptable range (e.g., 1000 bits processed per sample would be 100 mW here). To take a concrete example, commercial RFID tags consume ∼10 μW [110]. At a chip rate of 256 kbit/s (with a Miller encoding of 2), this yields 7.8×10^{-11} J/bit, which is ∼10 orders of magnitude higher than the Landauer limit. Applying current RFID technology to whole mouse brain recording at 1 kbit/s/neuron would thus draw ∼8 W of power. Therefore, at least 2–3 orders of magnitude reduction in power consumption will be necessary in order to apply embedded electronics for whole-brain neural recording.

Until recently, the energy efficiency of digital computing has scaled on an exponential improvement curve [108]. This was a consequence of Moore's law and Dennard scaling, where both the capacitance of each transistor and its associated interconnect, as well as the operating voltages, were reducing with the device dimensions. Unfortunately however, issues related to device variability and the 3D structures needed to maintain the on-to-off current ratio have largely stopped the reduction in effective capacitance per device; current devices are stuck at ∼100–200 aF for a minimum sized transistor. Furthermore, the exponential increase in leakage current that comes along with the scaling of the threshold voltage in this scenario has precluded substantial further decreases in voltage at a given performance level. Indeed, for the past several technology generations (since about 2005), CMOS devices have operated at a supply voltage of ∼1 V. While neural signal processing does not demand very stringent transistor speeds and so reductions below ∼1 V are certainly feasible, a fundamental limitation in scaling the supply voltage still remains. Specifically, CMOS has a well-defined minimum-energy per bit and an associated minimum-energy operating voltage that is defined by the tradeoff between static (leakage) and dynamic (switching) energy: as the operating voltage is decreased, the capacitive switching energy decreases, but the ratio of currents in the on and off states, $I_{\mathrm{off}}/I_{\mathrm{on}}$, increases exponentially, increasing the energy associated with leakage (this effect is independent of the threshold voltage in the sub-threshold regime). For practical circuits, the supply voltage that leads to this minimum energy is on the order of 300–500 mV, and thus supply voltage scaling will at most provide 3×–10× improvement in energy over today's designs. Thus, a paradigm shift in microelectronic hardware is needed to reduce power by several orders of magnitude if we are to approach the physical limits. Developing a switching device operating in the mV range, rather than the 1 V range of current transistors, would allow $(1\,\mathrm{V}/1\,\mathrm{mV})^2 = 10^6$ fold reduction in power consumption [105]. Electronic circuits constructed using analog techniques [111], which sometimes rely on bio-inspired computational architectures, show promise for reducing energy costs by up to five orders of magnitude [111–113], depending on the nature of the computation and the required level of precision.

Figure 4 shows the power consumption per bit processed for several technology classes as well as the corresponding total power consumption required for whole brain readout, assuming a minimal whole-brain bit rate of 100 Gbit/s.

4.3.2 Powering Embedded Devices

Embedded systems need power, which could be supplied via electromagnetic or acoustic energy transfer, or could be harvested from the local environment in the brain.

There are two key regimes for wireless electromagnetic power transfer: non-linear device rectification and photovoltaics. If the single-photon energy is sufficient to allow electrons to move from the valence to the conduction band — that is, band gap $< h\nu/q$, where

Figure 4. Energy cost of elementary operations across a variety of recording and data transmission modalities, expressed in units of the thermal energy (left axis) and as a power assuming 100 GHz switching rate (right axis). The Landauer limit of $k_B T \ln 2$ sets the minimum energy associated with a logically irreversible bit flip. The practical limit will likely lie in the tens of $k_B T$ per bit, comparable to the free energy release for hydrolysis of a single ATP molecule (or addition of a single nucleotide to DNA or RNA). The energy of a single infrared photon is $\sim 50\, k_B T$. Single gates in current CMOS chips dissipate $\sim 1 \times 10^5$–$10^6\, k_B T$ per switching event, including the capacitive charging of the wires interconnecting the gates (red curve). The switching energy for the gate, not including wires, is $\sim 100\times$ lower (blue curve). The power efficiency of CMOS has been on an exponential improvement trend due to the miniaturization of components according to Moore's law (data re-digitized from [107]), although power efficiency gains have slowed recently. Current RFID chips compute and communicate at $\sim 1 \times 10^9$–$10^{10}\, k_B T$ (> 10 pJ) per bit transmitted, while the total energy cost per floating point operation in a 2010 laptop was $\sim 1 \times 10^{12}\, k_B T$. The power associated with a minimal low-noise CMOS analog front end for signal amplification corresponds to ~ 500 mW at whole mouse brain scale. A single two-photon laser pulse at 0.1 nJ pulse energy corresponds to $\sim 1 \times 10^{10}\, k_B T$. For comparison, the 40 mW approximate maximal power dissipation of a neural recording setup, according to section 2 (Basic Constraints) above, with its equivalent per-bit energy of $\sim 1 \times 10^8\, k_B T$ at the minimal 100 Gbit/s bit rate.

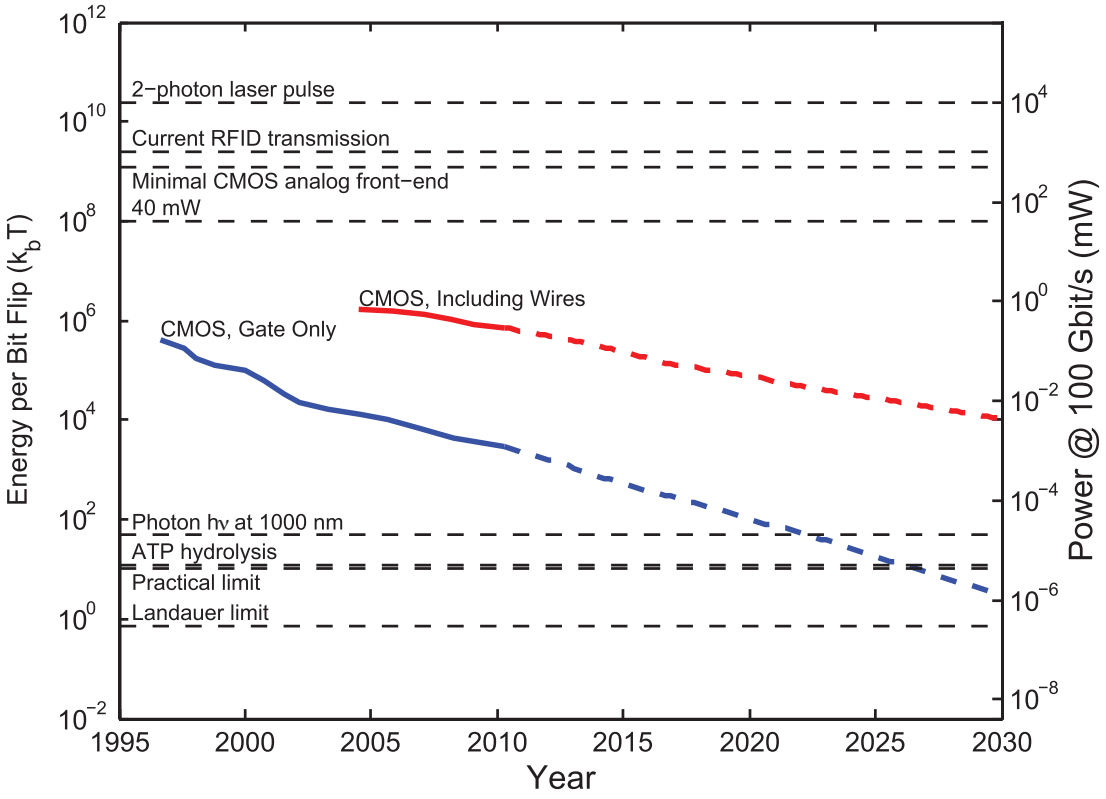

q is the electron charge, h is Planck's constant, and ν is the frequency of the photon — a photovoltaic effect can occur. Otherwise, electromagnetic energy is converted to voltage by an antenna and non-linear device rectification may occur.

In this regime (single photon energy much lower than the band gap), power conversion is governed by the total RF power and by the impedances of the antenna and the rectifier, rather than by the individual photon energy. For a monochromatic RF source, there is no thermodynamic or quantum limit to the RF to DC conversion efficiency, other than the resistive losses and threshold voltages for a semiconductor process. For rectification, when the input voltage to the rectifier is much higher than a semiconductor process threshold, conversion efficiencies of 85 % have been achieved [114]. At low input voltages relative to the semiconductor process threshold, efficiencies as high as 25 % and 2 μW load have been achieved (see [113] for an analysis of power efficiency). Ultimately, rectification improvements are dependent on the same improvements which will be needed for next-generation low-power computing: mV scale switching devices (promising research directions include tunnel FETs [115], electromechanical relays [116] and other options).

While efficient rectification is thus not a fundamental issue, capturing sufficient RF energy in the first place becomes increasingly challenging as microchips become smaller and more deeply embedded in tissue. Wireless electromagnetic power transfer imposes range constraints due to the loss in power density with distance. For directional power transfer, placing the receiver at the edge of the transmitter's near field (the Rayleigh distance $D^2/4\lambda$ where D is the transmitter aperture) has advantages in terms of energy capture efficiency [117], whereas for omni-directional antennas it is advantageous to place the receiver as close as possible to the transmitter. If embedded chips are oriented randomly with respect to the transmitter, the radiation patterns of their antennas cannot be highly directional, i.e., their gains G_r (a measure of directionality) must be close to one. In the far field, this lack of directionality limits power capture by the antenna (due antenna reciprocity [118]): the maximal power P_A available to the chip is

$$P_A = \frac{G_r P_{\text{rad}} \lambda^2}{4\pi}$$

where P_{rad} is the power density of radiation around the antenna, λ is the wavelength and $G_r \approx 1$ for a non-directional antenna [113].

It may be possible to power devices with pure magnetic fields (which are highly penetrant) using magneto-electric materials [119–122] or via near-field (non-radiative) inductive coupling, which is widely used in systems ranging from biomedical implants to electric toothbrushes. For the case of simple inductive coupling, however, the tiny cross-sections of micro-devices limit the amount of power which can be captured: a loop of 10 μm diameter in an applied field of 1 T switching at 1000 Hz produces an induced electromotive force of only 0.1 μV. Assuming a copper loop (∼17 nΩ m resistivity) with 1 μm × 1 μm cross-section and 40 μm length (around the outer edge of the chip) gives a power V^2/R of only ∼15 fW associated with the induced current. In general, the use of coupled high-Q resonators can increase the range and efficiency of near-field electromagnetic power transfer by orders of magnitude [123] compared to non-resonant inductive power transfer and may be particularly relevant for implanted devices [124]. Unfortunately, at the ∼10 μm length scale, the achievable on-chip inductances and capacitances are severely limited, which restricts the operating range of any resonant device to high frequencies $f_{\text{resonant}} = \frac{1}{2\pi\sqrt{LC}}$ which will be attenuated by tissue. Electromagnetic near-field power transfer though tissue to ultra-miniaturized microchips may thus be inefficient, again due to low capture efficiency of the applied fields by tiny device cross-sections.

Alternatively, if the photon energy is above the silicon band gap ($\lambda < \frac{hc}{qV_{\text{th}}} \approx 3$ μm or less for silicon), the chip is essentially acting as a photovoltaic cell. There is no thermodynamic or quantum limit to the conversion efficiency of light to DC electrical power for monochromatic sources, other than resistive losses and dark currents in the material (86 % in GaAs for example [125]). Again, however, capturing sufficient light becomes difficult for tiny devices. To supply 10 μW (typical of current wirelessly-powered RFID chips) photovoltaically to a 10 μm × 10 μm (cell sized) chip at 34 % photovoltaic efficiency requires a light intensity of ∼300 kW/m^2 at the chip, which is prohibitive. Furthermore, in the use of infrared light for photovoltaics, the penetration of the photons through tissue is decreased compared to radio frequencies.

Piezoelectric harvesting of ultrasound energy by micro-devices is a possibility. The efficiency of electrical harvesting of mechanical strain energy in piezoelectrics can be above 30 % for materials with high electromechanical coupling coefficients (e.g., PZT) [126, 127]. The losses in the piezoelectric transduction process are well described by models such as the KLM model [128, 129].

An alternative to wireless energy transmission is the local harvesting of biochemical energy carriers. Implanted neural recording devices could conceivably be powered by free glucose, the main energy source used by the brain itself. The theoretical maximum thermodynamic efficiency for a fuel cell in aqueous solution is equal to that of the hydrogen fuel cell: $\Delta G^0/\Delta H^0 = 83$ % at 25 °C. Furthermore, if glucose is only oxidized to gluconic acid, the Coulombic (electron extraction) efficiency is at most 8.33 % [130], which bounds the thermodynamic efficiency. The blood glucose concentration in rats has been measured at ∼7.6 mM, with an extracellular glucose concentration in the brain of ∼2.4 mM [131]. A hypothetical highly miniaturized neural recorder with a device area of 25 μm × 25 μm and efficiency of 80 %, processing a blood flow rate of ∼1 mm/s [132] could extract (80 %)(7.6 mM)(25 μm)^2(1 mm/s)(2880 kJ/mol) ≈

11 μW, which is sufficient for low-power device such as RFID chips [133]. Unfortunately, current non-microbial glucose fuel cells obtain only ~180 μW/cm^2 peak power and ~3.4 μW/cm^2 steady state power [130]. Thus there is a need for 10^4- and 10^6-fold improvements in peak and steady state power densities, respectively, for non-microbial glucose fuel cells to power brain-embedded electronics of the complexity of today's RFID chips (or better, the corresponding decrease in power requirements for the chips, as emphasized above).

4.3.3 Conclusions and Future Directions

The power consumption of today's microelectronic devices is more than 6 orders of magnitude higher than the physical limit for irreversible computing, and 2–3 orders of magnitude higher than would be permissible for use in whole brain millisecond resolution activity mapping, even under favorable assumptions on the required switching rates and neglecting both the power associated with noise rejection in the analog front end and the CMOS leakage current. Thus, the first priority is to reduce the power consumption associated with embedded electronics. In principle, methods such as infrared light photovoltaics, RF harvesting via diode rectification, or glucose fuel cells, could supply power to embedded neural recorders, but again, significant improvements in the power efficiency of electronics are necessary to enable this. Other potential energy harvesting strategies include materials/enzymes harnessing local biological gradients such in voltage, osmolarity, or temperature. An analysis of the energy transduction potential of each of these systems is beyond the scope of this discussion. Fortunately, with many orders of magnitude potential for improvement before physical limits are reached, we may expect that embedded nano-electronic devices will emerge as an energetically viable neural interfacing option at some point in the future.

4.4 Embedded Devices: Information Theory

Most recording methods envisioned thus far rely on the real-time transmission of neural activity data out of the brain. Physics and information theory impose fundamental limits on this process, including a minimum power consumption required to transmit data through a medium. The most basic of these results hold irrespective of whether the data transmission is wired or wireless, and regardless of the particular physical medium (optical, electrical, acoustic) used as the information carrier.

A communication "channel" is a set of transmitters and receivers that share access to a single physical medium with fixed bandwidth. The bandwidth is the range of frequencies present in the time-varying signals used to transmit information. In wireless communications, information is transmitted by modulating a carrier wave. To allow modulation, the frequency of the carrier wave must be higher than the bandwidth: for example, a 400 THz visible light wave may be modulated at a 100 GHz rate. The physical medium underlying a channel could be a wire (with a bandwidth set by its capacitive RC time constant), an optical fiber, free space electromagnetic waves over a certain frequency range, or other media.

As a concrete example, consider a police department with 100 officers, each possessing a hand-held radio. The radios transmit vocalizations by modulating an 80 MHz carrier wave at ~10 kHz. This constitutes a single shared communications channel with 10 kHz bandwidth. Simultaneously, the fire department may communicate via a separate channel, also with a bandwidth of ~10 kHz, by modulating a 90 MHz carrier wave. The channels are separate because modulation introduced into one does not affect the other. If the neighboring town's police department makes the mistake of also operating at 80 MHz carrier frequency, then they share a channel and conflicts will arise.

4.4.1 Power Requirements for Single-Channel Data Transmission

We first treat the case in which there is a single channel for transmitting data out of the brain. The Shannon Capacity Theorem [134] sets the maximal bit rate for a channel (assuming additive white Gaussian noise) to

$$R_{\max} = \mathrm{BW} \log_2 (1 + \mathrm{SNR})$$

where BW is the channel bandwidth and SNR is the signal-to-noise ratio. If there is only thermal noise the $\mathrm{SNR} = P/(N_0 \mathrm{BW})$, where N_0 is the thermal noise power spectral density of $k_B T$ W/Hz and $P = (\mathrm{PL})P_0$ is the power of the transmitted signals P_0, weakened by path loss PL. Therefore the transmitted power P_0 is lower-bounded:

$$P_0 > k_B T \ \mathrm{BW} \ \frac{2^{R_{\max}/\mathrm{BW}} - 1}{\mathrm{PL}}$$

as shown in Figure 5 (bottom). In a minimal model of a transmitter-receiver system, there thus exists a tradeoff between the required signal power and the bandwidth of the carrier radiation, due to the thermal noise floor, even in the absence of path loss (PL = 1).

Path loss weakens the proportion of the power that can reach the detector. Using the above equation, we can calculate, as a function of bandwidth, the power necessary to transmit a target whole-brain bit rate of 100 Gbit/s through a medium with path loss dependent on the carrier wavelength, as shown in Figure 5 (top).

Figure 5. Fundamental power requirements imposed by information theory on data transmission through a single (additive white Gaussian noise) channel with carrier frequency ν (an upper bound on the bandwidth), given thermal noise and path loss. Bottom: absorption length of water as a function of frequency (blue), minimal power to transmit data at 100, 1000 and 10 000 Gbit/s (green) as a function of frequency, assuming thermal noise but no path loss. Top: minimal power to transmit data at 100, 1000 and 10 000 Gbit/s as a function of frequency, assuming thermal noise and a path loss corresponding to the attenuation by water absorption over a distance of 2 mm. While formulated for a single channel, at certain wavelengths (e.g., RF) these factors also constrain multiplexed data transmissions between many transmitters and many receivers, depending on capacity of the system for spatial multiplexing. Horizontal dashed lines: 40 mW, the approximate maximal whole-brain power dissipation in steady state.

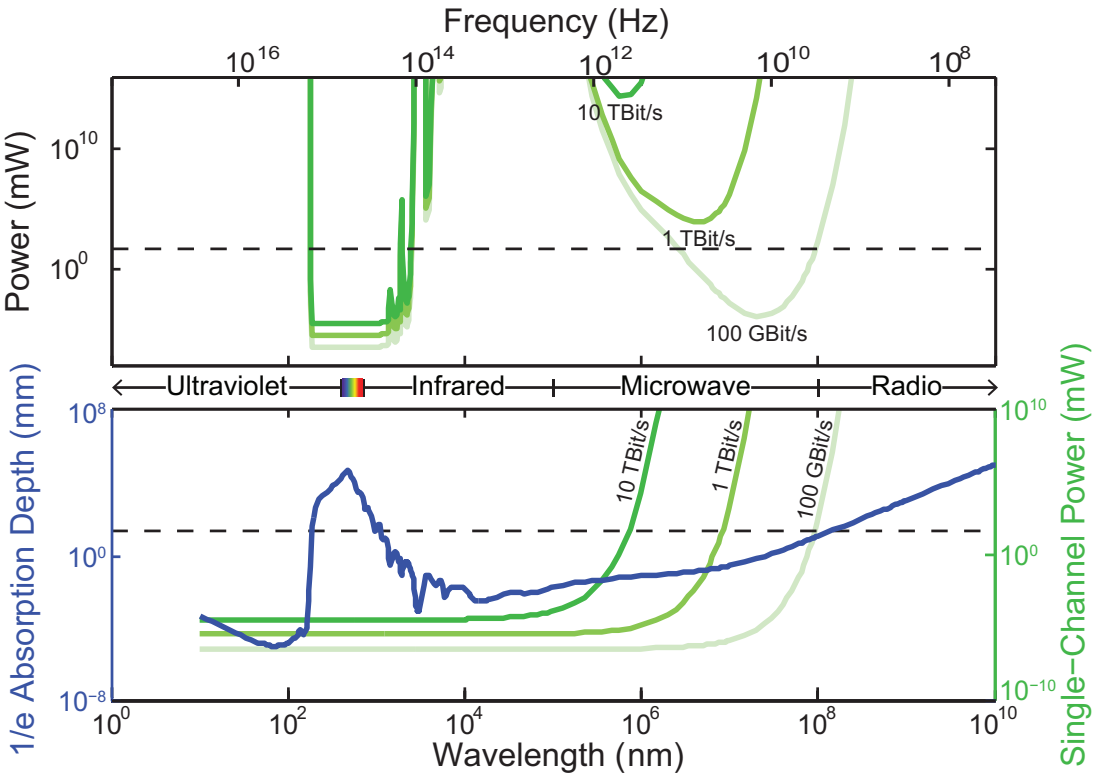

For RF wavelengths, the radiation penetrates deeply but the achievable data rates are low without excessive power consumption, due to the limited bandwidth. For wavelengths intermediate between RF and infrared, the penetration depth is low and power must be expended to combat these losses, despite the high carrier bandwidth. Only in the infrared and visible ranges do the tradeoffs between power, bandwidth and penetration depth allow transmission of > 100 Gbit/s out of the brain through a single channel without unacceptable power consumption.

The analysis above has ignored the effects of noise sources other than thermal noise, but many additional noise sources will increase the amount of power needed to transmit data, via a decrease in the SNR at fixed input power. For optical transmission in the brain, the noise is dominated by time-correlated "speckle noise" below 200 kHz, which arises mostly from local blood flow [135]. This correlated noise, which cannot be filtered by simple averaging, could be avoided by modulating optical signals at frequencies above 200 kHz.

4.4.2 Spatially Multiplexed Data Transmission

As discussed above, transmitting information through a single channel imposes direct limits on bit rate, carrier frequency and input power. However, it is conceivable to divide the data transmission burden over many independent channels, i.e., over many pairs of transmitters and receivers, each operating at lower bandwidth (e.g., at radio frequencies). Indeed, this would be optimal in a scenario where many embedded devices measure and then transmit the activities of nearby neurons. As a concrete example of such "spatial multiplexing," an effective capacity of 1 Tbit/s could conceivably be obtained by splitting the data over 1000 transmitter-receiver pairs each operating at 1 Gbit/s, with the transmitters arranged in a $10 \times 10 \times 10$ grid. Importantly, in order to exceed the above limits for single-channel data transmission, it must be possible for these transmitter receiver pairs to share the same bandwidth and operate simultaneously without conflicts, for example by modulating distinguishable carrier waves or by transferring data over separate wires. The conditions under which this may occur, however, can be counter-intuitive. For example, for antennas to operate independently, they must be spaced apart from one another by roughly a wavelength. For 10 GHz microwaves, the wavelength is $\sim$3 cm, so no more than a handful of microwave transmitters can co-occupy the mouse brain while operating independently.

Even with many non-independent transmitters co-occupying the brain and operating simultaneously over the same frequency spectrum, it may be possible under some conditions to "factor out" the effects of the coupling and allow an increase in channel capacity relative the single-channel result. To treat such scenarios, a generalization to Shannon's capacity theorem to multi-input-multi-output (MIMO) channels has shown that the maximal total data rate is

$$R_{\max} = \mathrm{BW} \cdot \log_2 \left| \boldsymbol{I} + (\mathrm{SNR}) \boldsymbol{H} \boldsymbol{H}^* \right|$$

where $\boldsymbol{I}$ is the identity matrix, $|\cdot|$ denotes the matrix determinant, $\boldsymbol{H}$ is the ($M \times N$ for N transmitters and M receivers) channel matrix giving the coupling between the vector of transmitted signals and the vector of received signals and $\boldsymbol{H}^*$ denotes the matrix adjoint of $\boldsymbol{H}$ [136]. The vector of received signals is then $\boldsymbol{y} = \boldsymbol{H}\boldsymbol{x} + \boldsymbol{n}$ where $\boldsymbol{x}$ is the vector of transmitted signals and $\boldsymbol{n}$ is a noise vector. Any matrix can be written as $\boldsymbol{H} = \boldsymbol{U}\boldsymbol{\Sigma}\boldsymbol{V}^*$ where $\boldsymbol{U}$ and $\boldsymbol{V}$ are unitary matrices, and $\boldsymbol{\Sigma}$ is a diagonal matrix whose elements are the *singular values* λ_i. One can re-write the above equation as

$$R_{\max} = \mathrm{BW} \cdot \sum_{i=1}^{\min(M,N)} \log_2 \left(1 + \mathrm{SNR} \cdot \lambda_i^2\right)$$

If the matrix $\boldsymbol{H}$ is of full rank, then the capacity for the multi-channel system can increase over the single-input-single-output (SISO) result by $\min(M,N)$ times [137]. Note that the rank of the matrix corresponds to the number of non-zero singular values, so an analysis of the singular values of channel matrices can inform us about the multiplexing capacity of the channel. Furthermore, this multiplexing capacity can in principle be achieved even when the transmitters are not in communication with each other, which could potentially be important for scenarios involving many brain embedded transmitters [138].

Transmission through a medium with negligible scattering is the simplest situation to analyze. In this case, evaluating the matrix $\boldsymbol{H}$ requires knowledge of the transmitter-transmitter, transmitter- receiver, and receiver-receiver distances, as well as the orientations and radiation patterns of the antennas (e.g., high gain antennas will have a highly directional radiation pattern). Depending on these factors, the beam from each transmitter will spread to impinge upon multiple receivers and the effective number of spatially independent beams will be reduced. With transmitter-transmitter and receiver-receiver distances larger than the wavelength, and highly directional antennas with appropriately chosen orientations, it is possible to increase the channel capacity linearly with $\min(M,N)$.

Random scattering, in a coherent disordered medium where the mean free-path ℓ is much larger than the wavelength λ and much smaller than the size of the disordered medium, is another condition where the matrix $\boldsymbol{H}$ is a random scattering matrix of full rank [139, 140]. Intuitively, for the case of two transmitters and two receivers separated by a disordered medium larger than the mean free path: if transmitter 1 is at least a mean-free path from transmitter 2 (or potentially as close as a few wavelengths [141]) the path

from transmitter 1 to receiver 1 and the path from transmitter 2 to receiver 2 would be uncorrelated with respect to one another (in terms of physical path, phase, amplitude fluctuations, and other properties). The rank of the matrix $\boldsymbol{H}$ would then be 2. Devising a code on the transmitter such that the receivers can distinguish between these two uncorrelated streams results in a doubling of the capacity, rather than simply averaging the noise floor, which would provide only a logarithmic capacity gain due to the increased SNR.

Thus, contrary to intuition, a high degree of random scattering can potentially be useful for data transmission, by enabling spatial multiplexing of channels. This idea has been demonstrated experimentally in the context of ultrasound transmissions [142]. Biological tissue in the infrared range is well described as such a random scattering medium (e.g., mean free path $\sim$200 μm at $\sim$800 nm *in vivo*). Therefore infrared light could be used for spatially multiplexed data transmission out of the brain. At wavelengths λ comparable to critical brain dimensions in the mouse, however, an insufficient number of scattering events will occur to create multiple independent pathways for N transmitters. Mathematically, the matrix $\boldsymbol{H}$ will have one highly dominant singular value and a number of much smaller remaining terms, such that the signals appearing at a receiver from two separate transmitters will be highly linearly dependent, differing by only a small phase angle. Therefore, there will be no capacity gain from multiple transmitters, and distinct transmitters will effectively share a single channel (reducing to the SISO result).

Little is known about the biological interaction with electromagnetic fields at wavelengths much shorter than the critical brain dimensions but beyond the infrared, approximately 100 GHz ($\sim$3 mm) to 100 THz ($\sim$3 μm) in the mouse. If multiple scattering occurs and the absorption is low, this may also be a regime conducive to MIMO communications [143]. Efficiently generating and processing radiation in this regime by embedded devices is an outstanding problem, however. The so-called "THz-gap" [144] exists because (moving towards higher frequencies starting from DC electronics), parasitic capacitances and passive losses limit the maximum frequency at which a field-effect transistor (FET) may oscillate and on the other hand (moving downward in frequency starting from optics), the band-gaps of opto-electronic devices limit the minimum frequency at which quantum transitions occur. Thus there is no high-power, low-cost, portable, room temperature THz source available. Advances in THz light generation, e.g. through the use of tunneling transistors, could be enabling.

4.4.3 Ultrasound as a Data Transmission Modality

An important caveat to these conclusions on wireless data transfer occurs if we consider the use of ultrasound rather than electromagnetic radiation Because the speed of sound is dramatically slower than that of light, the wavelength of 10 MHz ultrasound is only $\sim$150 μm (approximating the speed of sound in brain as the speed of sound in water, $\sim$1500 m/s). Thus, many 10 MHz ultrasound transmitters/receiver could be placed inside a mouse brain while maintaining their spatial separation above the wavelength, and a linear scaling of the MIMO channel capacity with the number of devices is likely possible in this regime, assuming that appropriate antenna gains and orientations can be achieved inside brain tissue. Beam orientation could present a challenge if micro-devices are oriented randomly after implantation. With an attenuation of 0.5 dB/(cm MHz) [145], the attenuation at 10 MHz is only 5 dB/cm. Thus ultrasound-based transmission of power and data from embedded recording devices may be viable.

In contrast, direct imaging of neural activity by ultrasound (e.g., using contrast agents which create local variations in tissue elastic modulus or density) may be more difficult. The wavelength of 100 MHz ultrasound is $\sim$15 μm, providing a theoretical diffraction limited spatial resolution that would be sufficient for resolving neuronal somas. Practical transducer designs operating at this frequency achieve axial and lateral resolutions in the range of 15–60 μm [146]. However, at these frequencies, power is attenuated by brain tissue with a coefficient of $\sim$50 dB/cm [145] (10^5-fold attenuation per cm), which imposes a penetration limit (e.g., for measurements with a dynamic range of 80 dB [146]). Attenuation of ultrasound by bone is stronger still, at 22 dB/(cm MHz) [145]. Attenuation could therefore limit the use of ultrasound as a high-resolution neural recording modality in direct imaging modes, but multiplexed transmission of lower-frequency ultrasound from embedded devices could sidestep this issue.

4.4.4 Conclusions and Future Directions

Physics and information theory impose a tradeoff between bandwidth and power consumption in sending data through any communication channel. Considering only thermal noise and no path loss, achieving 100 Gbit/s data rates through a single channel necessitates either a bandwidth above a few GHz or a transmitted power above $\sim$100 mW, the latter of which may be prohibitive from a heat dissipation perspective if the signals are to be generated by dissipative microelectronic devices. Researchers have proposed to use thousands or millions of tiny [147] wireless transmitters embedded in the brain to transmit local neural activity measurements to an external receiver via microwave radiation [148]. However, based on the above power-bandwidth tradeoff, this will require a bandwidth above a few GHz. At the corresponding carrier frequencies, the penetration depth of the microwave radiation drops significantly, requiring increased power to combat the resulting signal loss. While one might hope that multiple independent channels could be multiplexed inside the brain, reducing the bandwidth and power requirements for each individual channel, the long wavelengths of microwave radiation compared to the mouse brain diameter suggest that such channels cannot be independent, as is confirmed by an analysis of the multi-input-multi-output (MIMO) channel capacity for this scenario. Therefore, radio-frequency electromagnetic transmission

of whole brain activity data from embedded devices does not appear to be a viable option for brain activity mapping. On the other hand, an analysis of the channel capacity for IR transmissions in a diffusive medium suggests that, because of its high frequency and decent penetration depth, infrared radiation may provide a viable substrate for transmitting activity data from embedded devices. For example, data could be transmitted via modulating the multiple-scattering speckle pattern of infrared light by varying the backscatter from an embedded optical device, such as an LCD pixel, in an activity-dependent fashion. Because the speckle pattern is sensitive to the motion of a single scatterer [141], coherent multiple scattering could effectively act as an optical amplifier and as a means to create independent communication pathways. Furthermore, multiplexed data transmission via ultrasound is likely possible because of its short wavelength in tissue at reasonable carrier frequencies. It may also be of interest to explore network architectures [149] in which data is transmitted at low transmit power over short distances via local hops between neighboring nodes capable of signal restoration.

4.5 Magnetic Resonance Imaging

Magnetic resonance imaging (MRI) uses the resonant behavior of nuclear spins in a magnetic field to non-invasively probe the spatiotemporally varying chemical and magnetic properties of tissues. Although originally conceived as a means to image anatomy, MRI can be used to observe neural activity provided such activity is reflected in dynamic changes in local chemistry or magnetism.

In an MRI study, a strong static field ($B = 1$–$15\,\mathrm{T}$) is applied to polarize nuclear spins (usually ^{1}H), causing them to resonate at a field-dependent Larmor frequency

$$f = \frac{\gamma}{2\pi} B$$

where γ is the gyromagnetic ratio of the nucleus (267.522 MHz/T for ^{1}H [150]). To obtain positional information, spatial field gradients are applied such that nuclei at different positions in the sample resonate at slightly different frequencies. Sequences of RF pulses and gradients are then applied to the sample, eliciting resonant emissions that contain information about spins' local chemical environment, magnetic field anisotropy and various other properties.

Most functional studies rely on dynamic changes in two forms of relaxation experienced by RF-excited spins. The first form results from energy dissipation through interactions with other species (e.g. other spins or unpaired electrons), causing the spins to recover their lowest energy state on a timescale T_1 of 100–1000 ms [151]. The second form of relaxation reflects the dephasing of spin signals in a given sampling volume (voxel) over a timescale T_2 of 10–100 ms [152] due to non-uniform Larmor frequencies caused, e.g., by the presence of local magnetic field inhomogeneities.

In blood-oxygen level dependent functional MRI (BOLD-fMRI) — the most widely used form of neural MR imaging — increased neural activity in a given brain region alters the vascular concentration of paramagnetic deoxy-hemoglobin, which affects local magnetic field homogeneity and thereby alters T_2. Although the existence of this paramagnetic reporter of oxygen metabolism is fortuitous, the data it provides is only an indirect readout of neural activity, which is limited in its spatial and temporal resolution to the dynamics of blood flow in the brain's capillary network (1–2 s). A significant area of current and future work is aimed at developing new molecular reporters that can be introduced into the brain to transduce aspects of neural signaling such as calcium spikes and neurotransmitter release into MRI- detectable magnetic or chemical signals [153–155].

4.5.1 Spatiotemporal Resolution

The temporal resolution of MRI is limited by the dynamics of spin relaxation. For sequential MR signal acquisitions to be fully independent, spins must be allowed to recover their equilibrium magnetization on the timescale of T_1 (100–1000 ms). However, if local T_1 is static its pre-mapping could enable temporally variant T_2 effects to be observed at refresh rates on the faster T_2 timescale (10–100 ms) [152]. It may also be possible to detect events that occur on a timescale shorter than T_1 and T_2, if the magnitude of the resulting change in spin dynamics overcomes the lack of independence between acquisitions. Note that these limitations on the repetition time of the underlying pulse sequence are not eliminated by "fast" pulse sequences such as echo-planar imaging (EPI) [156] and fast low-angle shot (FLASH) [157] or by the use of multiple detector coils [158]. These techniques accelerate the acquisition of 2D and 3D images, but still require spins to be prepared for readout.

The spatial resolution of current MRI techniques is limited by the diffusion of water molecules during the acquisition time [159], since contrast at scales above the diffusion length will be attenuated by diffusion. The RMS distance of a water molecule from its origin, after diffusing in 3D for a time T_{acq}, is

$$d_{\mathrm{rms}} = \sqrt{6 D_{\mathrm{water}} T_{\mathrm{acq}}}$$

where $D_{\mathrm{water}} = 2300\,\mu\mathrm{m}^2/\mathrm{s}$ is the self-diffusion coefficient of water. For $T_{\mathrm{acq}} \approx 100\,\mathrm{ms}$, $d_{\mathrm{rms}} \approx 37\,\mu\mathrm{m}$, which sets the approximate spatial resolution. For ultra-short acquisitions at $T_{\mathrm{acq}} \approx 10\,\mathrm{ms}$, $d_{\mathrm{rms}} \approx 12\,\mu\mathrm{m}$.

More technically, as described above, MRI uses field gradients to encode spatial positions in the RF frequency (wavenumber) components of the emitted radiation. The quality of the reconstruction of frequency space thus limits the achievable spatial resolution. Δt, the sampling interval of the detector, and the field gradient G, determine the wavenumber increment as

$$\Delta k = \gamma G \Delta t$$

The spatial resolution is then given by [159]:

$$\Delta x_{k\text{-space}} = \frac{\pi}{\frac{T_{\text{acq}}}{\Delta t}\Delta k} = \frac{\pi}{T_{\text{acq}}\gamma G}$$

Note that it is the gradient field, not the polarizing field B_0, which determines the resolution. For a gradient field of 100 mT/m and an acquisition time of 100 ms

$$\Delta x_{k\text{-space}} = \frac{\pi}{(100\,\text{ms})\,(267\,\text{MHz/T})\,(100\,\text{mT/m})} \approx 1.17\,\mu\text{m}$$

Furthermore, due to relaxation, the emissions from a spin at a given position do not constitute a pure tone with a well-defined frequency. Instead, each spin exhibits a frequency spread, which gives rise to a spatial resolution [159]:

$$\Delta x_{\text{relaxation}} = \frac{2}{\gamma G T_2^*}$$

where T_2^* is the shortest relaxation time. Assuming $T_2^* = 5$ ms and $G = 100$ mT/m, gives

$$\Delta x_{\text{relaxation}} \approx 14\,\mu\text{m}$$

Therefore, for water protons, the resolution limit is set by diffusion over ~100 ms acquisition timescales. For other spin species (e.g., with lower diffusion rate), it may be possible to achieve resolutions limited by frequency discrimination.

Notably, there exists a practical trade-off between spatial resolution, temporal resolution, and sensitivity (SNR). In particular, to achieve high spatial resolution, it is necessary to densely sample k-space. Fast sampling sequences such as FLASH and EPI achieve speed by sampling each point of k-space using less signal and often at a lower resolution. Even at high field strengths (11.7 T), this tradeoff results in practical EPI-fMRI with a spatial resolution of 150 μm × 150 μm × 500 μm and a temporal resolution of 200 ms [160]. Achieving much higher spatial resolutions requires longer acquisitions and/or lower temporal sampling. For example, achieving a 20 μm anatomical resolution in MRI of *Drosophila* embryos required 54 minutes for a small field of view of 2.5 mm × 2.5 mm × 5 mm [161]. Furthermore, the flies were administered paramagnetic gadolinium chelates to shorten T_1 and thereby the acquisition time. Separately, frame rates of 50 ms have been obtained for dynamic imaging of the human heart, but required the use of strong priors to reduce data collection requirements [162].

4.5.2 Energy Dissipation

Energy is dissipated into the brain when the excited spins relax to their equilibrium magnetization in the applied field. The energy associated with this relaxation is of order the Zeeman energy:

$$\Delta E_{\text{Zeeman}} = \frac{\gamma}{2\pi} h B_0$$

To obtain an upper bound on the heat dissipation of MRI, we first assume that the brain is entirely water, that every proton spin is initially aligned by the field and then excited by the RF pulse, and that all spins relax during a T_1 relaxation time of ~600 ms. In this scenario, even an applied field of as high as ~200 T would generate dissipation within the ~50 mW energy dissipation limit. In reality, the energy dissipation is 4–5 orders of magnitude smaller, because only a tiny fractional excess of the spins are initially aligned by the field (~1×10^{-5} for fields on the order of 1 T). Therefore, thermal dissipation associated with spin excitation in MRI is unlikely to cause problems unless field strengths much greater than the largest currently fields used (~20 T) are invoked, or spins with much higher gyromagnetic ratios are used.

Practically, the main energy consideration in MRI is the absorption by tissues of RF energy applied during imaging pulse sequences and the switching of magnetic field gradients. Such absorption is often calculated through numerical solutions of the Maxwell Equations taking into account the precise geometry, tissue properties and applied fields for a particular experimental setup [163]. The typical specific absorption rate (SAR) is well under 10 W/kg (or 5 mW per 500 mg), and is restricted by the FDA to less than 3 W/kg for human studies.

4.5.3 Imaging Agents

All the preceding discussion about spatiotemporal resolution presumes the existence of local time-varying signals (e.g., changes in T_1 or T_2) corresponding to the dynamics of neural activity. Such signals are not naturally present in the brain with the exception of the hemodynamic BOLD response, the limitations of which are discussed above (although there have been studies working towards direct detection of the minute neuronal magnetic fields associated with action potentials by MRI [164]). In the past 15 years, efforts have been undertaken to develop chemical and biomolecular imaging agents that can be introduced into the brain to produce MRI detectable signals corresponding to specific aspects of neural function (analogously to fluorescent dyes and proteins). Notable examples include T_1 and T_2 sensors of calcium [165, 166] and a T_1 sensor of neurotransmitter release [153]. Depending on their mode of action, these imaging agents can provide temporal resolutions ranging from 10 ms to 10 s [167]. However, a major current limitation for fast agents is the requirement that they be present in tissues at μM concentrations, posing major challenges for delivery and genetic expression.

Figure 6 shows the achievable temporal resolution for various classes of activity-dependent MRI contrast agents as well as the spatial resolution limit due to water proton diffusion.

Figure 6. Key factors determining the spatiotemporal resolution of dynamic MRI imaging. (a) Temporal resolution and contrast agent concentration allowing > 5 % contrast, for different classes of dynamic MRI contrast agent (reproduced from [167], with permission). (b) Diffusion limited spatial resolution for water proton MRI as a function of temporal resolution.

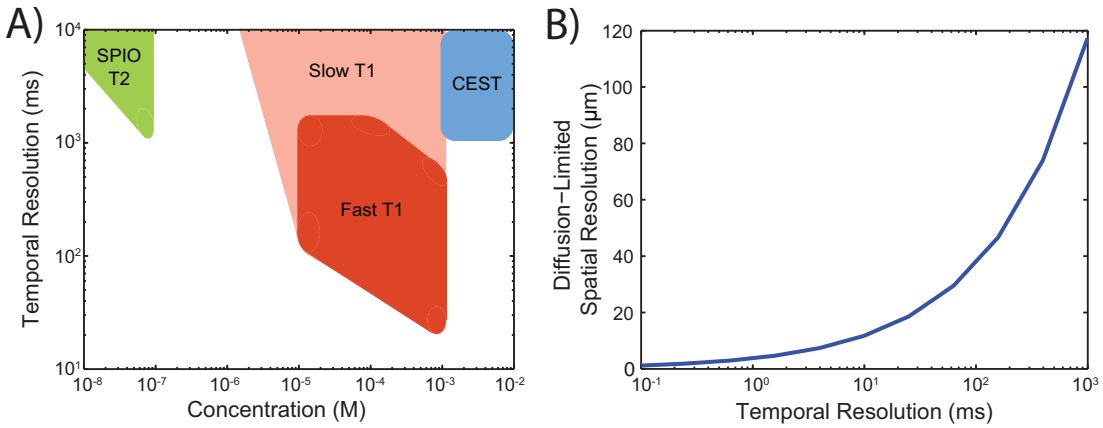

4.5.4 Conclusions and Future Directions

Current MRI techniques rely on the excitation of proton spins in water, however, and are thus limited to imaging at > 100 ms timescales unless SNR is severely compromised, due to the low polarizability and long T_1 relaxation time of proton spins. There is also a spatial resolution limit of tens of microns over these timescales due to water's fast diffusion. Methods which couple neural activity to non-diffusible, highly polarized spins could in principle ameliorate this situation.

4.6 Molecular Recording

An alternative to electrical, optical or MRI recording is the local storage of data in molecular substrates. Each neuron could be engineered to write a record of its own time-varying electrical activities onto a biological macromolecule, allowing off-line extraction of data after the experiment. Such systems could, in principle, be genetically encoded, and would thus naturally record from all neurons at the same time.

One proposed implementation of such a "molecular ticker tape" would utilize an engineered DNA polymerase with a Ca^{2+}-sensitive or membrane-voltage-sensitive error-rate [3] to record time-varying neural activities onto DNA [4] as patterns of nucleotide misincorporations relative to a known template DNA strand (for alternative local recording techniques see [168, 169]). The time-varying signal would later be recovered by DNA sequencing and subsequent statistical analysis [4]. DNA polymerases found in nature can add up to ∼1 000 nucleotides per second [170], and certain non-replicative polymerases such as DNA polymerase ι have error rates of > 70 % on template T bases [171]. Similar strategies could be implemented using RNA polymerases or potentially using other enzyme/hetero-polymer systems.

4.6.1 Spatiotemporal Resolution

Polymerases proceed along their template DNA strands in a stochastic, thermally driven fashion; thus, polymerases that are initially synchronized will de-phase with respect to one another over time, occupying a range of positions on their respective templates. The rate of this de-phasing is a key parameter governing the temporal resolution of molecular recording. By averaging over many (e.g., hundreds to thousands) of simultaneously replicated templates, it is theoretically possible to precisely associate nucleotide misincorporations with the times at which these misincorporations occurred, and thus to obtain recordings of the cation concentration at high temporal resolution. Furthermore, the development of mechanisms to improve synchronization of the ensemble of polymerases within each cell, or to encode time-stamps into the synthesized DNA (e.g., molecular clocks), could improve temporal resolution and decrease the number of required template strands per neuron. Mutation-based molecular clocks over evolutionary timescales are widely used in the field of phylogenetics [172], and new tools from synthetic biology [173] and optogenetics or thermogenetics [174] also suggest strategies for building molecular clocks on faster timescales.

An analysis of the projected temporal resolution of molecular ticker-tapes as a function of polymerase biochemical parameters can be found in [4]. This work suggests that molecular ticker tapes require synchronization mechanisms if they are to record at < 10 ms temporal resolution for durations longer than seconds, even when 10 000 templates per cell are recorded simultaneously, unless engineered polymerases with kinetic parameters beyond the limits of those found in nature can be developed. Recording at lower temporal resolutions, however, appears feasible using naturalistic biochemical parameters, even in the absence of synchronization mechanisms.

4.6.2 Energy Dissipation

Nucleotide metabolism DNA polymerization imposes a metabolic load on the cell. Replication of the 3 billion bp human genome takes approximately eight hours in normally dividing cells, which equates to a nucleotide incorporation rate of ~ 100 kHz. Therefore, in order not to exceed the metabolic rates associated with normal genome replication, molecular ticker tapes operating at 1 kHz polymerization speed [170] would be limited to approximately 100 simultaneously replicated templates per cell. Even more recordings would be possible for RNA ticker tapes. The mammalian cell polymerizes at least 10^{11} NTPs per 16-hour cell cycle (data from HeLa cells) [175]. Therefore, $\sim$1 700 RNA tickertapes, each operating at 1 kHz, could be placed in a cell before generating a metabolic impact equal to that of the cell's baseline transcription rate. While these comparisons to baseline physiological levels are reasonable guidelines, it is likely that a neuron can support higher metabolic loads associated with larger numbers of templates. The maximal rate of neuronal aerobic respiration is $\sim$5 fmol of ATP minute via oxidative respiration (see the section on bio-luminescence). Assuming $\sim$1 ATP equivalent consumed per nucleotide incorporation, if neuronal metabolism were entirely dedicated to polymerization, it could support the incorporation of up to 6×10^9 nucleotides per minute, or 10^5 simultaneously replicated DNA templates at 1 kHz.

Power dissipation Normal DNA and RNA synthesis do not produce problematic energy dissipation and molecular tickertapes will likewise not be highly dissipative, at least in the regime where nucleic acid polymerization rates do not exceed those associated with genome replication or transcription.

4.6.3 Volume Displacement

The nucleus of a neuron occupies $\sim$6 % of a neuron's volume ($(4\,\mu m)^3/(10\,\mu m)^3$). Ticker tapes operating at 1 kHz with 10 000 simultaneously replicated templates could record for 300 seconds before the total length of DNA synthesized equals the human genome length. In the case of RNA polymerase II-based transcription, 2.75 h of recording by 10 000 recorders is required to reach the net transcript length in the cell. Therefore, with appropriate mechanisms to fold/pack the nucleic acids generated by molecular ticker tapes, they would not impose unreasonable requirements on cellular volume displacement over minutes to hours.

4.6.4 Conclusions and Future Directions

Molecular recording of neural activity has the advantages of inherent scalability, single-cell precision, and low energy and volume footprints. Making molecular recording work at temporal resolutions approaching 1 kHz, however, will require multiple new developments in synthetic biology, including protein engineering to create a fast polymerase (> 1 kHz) that strongly couples proxies for neural activity to nucleotide incorporation probabilities. An attractive potential payoff from molecular approaches to activity mapping is the prospect of seamlessly combining — within a single brain — the readout of activity patterns with the readout of structural connectome barcodes [176], transcriptional profiles (cell type information) or other (epi-)genetic signatures which are accessible via high-throughput nucleic acid sequencing.

5 Discussion

We have analyzed the physical constraints on scalable neural recording for selected modalities of measurement, data storage, data transmission and power harvesting. Each analysis is based on assumptions – about the brain, device physics, or system architecture – which may be violated. Understanding these assumptions can point towards strategies to work around them, and in some cases we have suggested possible directions for such workarounds. Even valid assumptions about natural brains may be subject to modification through synthetic biology or external perturbation. Notably, methods for rapidly removing heat from the brain could be important for supporting a range of highly dissipative recording modalities, while assumptions about transmission bandwidth may be relaxed if some information is stored locally and read out after the fact.

We have not considered all possible recording modalities here. For example, modalities like X-ray imaging have been used on live cells [177] and might find use in neural recording if suitable contrast agents could be devised. X-rays interact with electron shells via photoelectric absorption and Compton scattering and with band structure in materials. X-ray phosphors utilize substitutions in an ionic lattice to generate visible or UV light emission upon X-ray absorption [178]. In principle, some of these mechanisms could be engineered as neural activity sensors, e.g., in an absorption-contrast mode suitable for tomographic reconstruction [179]. Alternatively, electron spin resonance (ESR) operates at $\sim$100$\times$ higher Larmor frequency compared to proton MRI, which improves polarizability of the spins. Due to Pauli exclusion, use of this technique requires an indicator with unpaired electrons. These can be found in nitrogen vacancy diamond nano-crystals [180] (nano-diamonds), which are also sensitive to voltage [181] and to magnetic fields [182], and are amenable to optical readout and control of the spin state.

Our analysis illustrates challenges and opportunities [183] for technology development. While we have shown that MRI is limited by the diffusion of water, using non-diffusible spins could in principle allow micron resolutions. While light scattering creates severe limitations on optical imaging, and multi-photon approaches are highly dissipative, embedded optical microscopies or novel fluorescent or bio-luminescent indicators (e.g., operating in the infrared) could overcome these limits. Novel contrast agents that exploit unused parts of the EM spectrum could allow entirely new forms of imaging. Ultra-low-power electronics is required to perform recording locally, but molecular recording devices could sidestep power constraints on electronics, at the cost of increased engineering complexity. New signal processing architectures such as compressive sensing could reduce bandwidth requirements and inspire new microscope designs. Hybrid techniques such as photo-acoustic [184] or ultrasound-encoded optical [82] microscopies could result in performance greater than the sum of the component technologies. Combining activity information with structural information could allow static and dynamic information to disambiguate one another.

Our goal here has not been to pick winners, but to aid a broad community in analyzing the problem. A challenge of this magnitude requires a return to first principles, and a fundamental reconsideration of the architectures of neural recording systems, not just incremental improvement of existing methods. We hope that knowledge of the constraints governing scalable neural recording will enable the invention of entirely new, transformative approaches.

6 Acknowledgments

We thank K. Esvelt for helpful discussions on bioluminescent proteins; D. Boysen for help on the fuel cell calculations; R. Tucker and E. Yablonovitch (http://www.e3s-center.org) for helpful discussions on the energy efficiency of CMOS; C. Xu and C. Schaffer for data on optical attenuation lengths; T. Dean and the participants in his CS379C course at Stanford/Google, including Chris Uhlik and Akram Sadek, for helpful discussions and informative content in the discussion notes (http://www.stanford.edu/class/cs379c/); and R. Koene, S. Rezchikov, A. Bansal, J. Lovelock, A. Payne, R. Barish, N. Donoghue, J. Pillow, W. Shih and P. Yin for helpful discussions.

A. Marblestone is supported by the Fannie and John Hertz Foundation fellowship. D. Dalrymple is supported by the Thiel Foundation. K. Kording is funded in part by the Chicago Biomedical Consortium with support from the Searle Funds at The Chicago Community Trust. E. Boyden is supported by the National Institutes of Health (NIH), the National Science Foundation, the MIT McGovern Institute and Media Lab, the New York Stem Cell Foundation Robertson Investigator Award, the Human Frontiers Science Program, and the Paul Allen Distinguished Investigator in Neuroscience Award. B. Stranges, B. Zamft, R. Kalhor and G. Church acknowledge support from the Office of Naval Research and the NIH Centers of Excellence in Genomic Science. M. Shapiro is supported by the Miller Research Institute, the Burroughs Wellcome Career Award at the Scientific Interface and the W.M. Keck Foundation.

References

[1] **Alivisatos** A Paul, Miyoung Chun, George M Church, Ralph J Greenspan, Michael L Roukes, and Rafael Yuste. "The brain activity map project and the challenge of functional connectomics," *Neuron* 74.6 (2012), 970–4, URL: http://academiccommons.columbia.edu/catalog/ac:147969 (cited on pp. 1, 9).

[2] **Stevenson** Ian H. and Konrad P. Kording. "How advances in neural recording affect data analysis," *Nature Neuroscience* 14 (online Jan. 26, 2011), 139–42, DOI: 10.1038/nn.2731 (cited on p. 1).

[3] **Zamft** Bradley M., Adam H. Marblestone, Konrad P. Kording, Daniel Schmidt, Daniel Martin-Alarcon, et al. "Measuring cation dependent DNA polymerase fidelity landscapes by deep sequencing," *PLoS ONE* 7.8 (Aug. 22, 2012), e43876, DOI: 10.1371/journal.pone.0043876 (cited on pp. 1, 2, 22).

[4] **Glaser** Joshua I., Bradley M. Zamft, Adam H. Marblestone, Jeffrey R. Moffitt, Keith Tyo, et al. "Statistical analysis of molecular signal recording," *PLoS Computational Biology* (2013), DOI: 10.1371/journal.pcbi.1003145 (cited on pp. 1, 2, 22, 23).

[5] **Kording** Konrad P. "Of toasters and molecular ticker tapes," *PLoS Computational Biology* 7.12 (Dec. 29, 2011), e1002291, DOI: 10.1371/journal.pcbi.1002291 (cited on pp. 1, 2).

[6] **Ahrens** Misha B., Michael B. Orger, Drew N. Robson, Jennifer M. Li, and Philipp J. Keller. "Whole-brain functional imaging at cellular resolution using light-sheet microscopy," *Nature Methods* 10 (online Mar. 18, 2013), 413–20, DOI: 10.1038/nmeth.2434 (cited on pp. 2, 9).

[7] **Ziv** Yaniv, Laurie D. Burns, Eric D. Cocker, Elizabeth O. Hamel, Kunal K. Ghosh, et al. "Long-term dynamics of CA1 hippocampal place codes," *Nature Neuroscience* 16 (online Feb. 10, 2013), 264–6, DOI: 10.1038/nn.3329 (cited on p. 2).

[8] **Vincent** Trevor J., Jonathan D. Thiessen, Laryssa M. Kurjewicz, Shelley L. Germscheid, Allan J. Turner, et al. "Longitudinal brain size measurements in APP/PS1 transgenic mice," *Magnetic Resonance Insights* 4 (Oct. 2010), 19–26, DOI: 10.4137/MRI.S5885 (cited on p. 3).

[9] **Azevedo** Frederico A. C., Ludmila R. B. Carvalho, Lea T. Grinberg, José Marcelo Farfel, Renata E. L. Ferretti, et al. "Equal numbers of neuronal and nonneuronal cells make the human brain an isometrically scaled-up primate brain," *Journal of Comparative Neurology* 513.5 (Feb. 2009), 532–41, DOI: 10.1002/cne.21974 (cited on p. 3).

[10] **Allen** John S., Hanna Damasio, and Thomas J. Grabowski. "Normal neuroanatomical variation in the human brain: an MRI-volumetric study," *American Journal of Physical Anthropology* 118.4 (Aug. 2002), 341–58, DOI: 10.1002/ajpa.10092 (cited on p. 3).

[11] **Sarpeshkar** Rahul. *Ultra Low Power Bioelectronics: Fundamentals, Biomedical Applications, and Bio-inspired Systems*, New York: Cambridge University Press, 2010, 747–8, URL: http://www.amazon.com/dp/0521857279/ (cited on p. 3).

[12] **Herculano-Houzel** Suzana. "Scaling of brain metabolism with a fixed energy budget per neuron: implications for neuronal activity, plasticity, and evolution," *PLoS ONE* 6 (2011), e17514, DOI: 10.1371/journal.pone.0017514 (cited on p. 3).

[13] **Speakman** John R. "Measuring energy metabolism in the mouse — theoretical, practical, and analytical considerations," *Frontiers in Integrative Physiology* 4.34 (Mar. 14, 2013), DOI: 10.3389/fphys.2013.00034 (cited on pp. 3, 11).

[14] **Gittis** Aryn H., Setareh H. Moghadam, and Sascha du Lac. "Mechanisms of sustained high firing rates in two classes of vestibular nucleus neurons: differential contributions of resurgent Na, Kv3, and BK currents," *Journal of Neurophysiology* 104.3 (June 2010), 1625–34, DOI: 10.1152/jn.00378.2010 (cited on p. 3).

[15] **Schneidman** Elad, Michael J Berry, Ronen Segev, and William Bialek. "Weak pairwise correlations imply strongly correlated network states in a neural population," *Nature* 440.7087 (2006), 1007–12 (cited on p. 3).

[16] **Markram** Henry, Wulfram Gerstner, and Per Jesper Sjöström. "A history of spike-timing-dependent plasticity," *Frontiers in synaptic neuroscience* 3 (2011) (cited on p. 3).

[17] **Babadi** Baktash and Larry F. Abbott. "Pairwise analysis can account for network structures arising from spike-timing dependent plasticity," *PLoS Comput Biol* 9.2 (Feb. 2013), e1002906, DOI: 10.1371/journal.pcbi.1002906 (cited on p. 3).

[18] **Dobbing** John and Jean Sands. "Quantitative growth and development of human brain," *Archives of Disease in Childhood* 48.10 (Oct. 1973), 757–67, DOI: 10.1136/adc.48.10.757 (cited on p. 3).

[19] **Fatouros** Panos P. and Anthony Marmarou. "Use of magnetic resonance imaging for in vivo measurements of water content in human brain: method and normal values," *Journal of Neurosurgery* 90.1 (Jan. 1999), 109–15, DOI: 10.3171/jns.1999.90.1.0109 (cited on p. 3).

[20] **Wilt** Brian A., Laurie D. Burns, Eric Tatt Wei Ho, Kunal K. Ghosh, Eran A. Mukamel, and Mark J. Schnitzer. "Advances in light microscopy for neuroscience," *Annual Review of Neuroscience* 32.1 (2009), PMID: 19555292, 435–506, DOI: 10.1146/annurev.neuro.051508.135540 (cited on pp. 3, 9).

[21] **Kou** Linhong, Daniel Labrie, and Petr Chylek. "Refractive indices of water and ice in the 0.65- to 2.5-μm spectral range," *Applied Optics* 32.19 (July 1, 1993), 3531–40, DOI: 10.1364/AO.32.003531 (cited on p. 3).

[22] **Horton** Nicholas G., Ke Wang, Demirhan Kobat, Catharine G. Clark, Frank W. Wise, et al. "*In vivo* three-photon microscopy of subcortical structures within an intact mouse brain," *Nature Photonics* 7 (online Jan. 20, 2013), 205–9, DOI: 10.1038/nphoton.2012.336 (cited on pp. 3, 9).

[23] **Gabriel** S, R.W. Lau, and C Gabriel. "The dielectric properties of biological tissues: iii. parametric models for the dielectric spectrum of tissues," *Phys. Med. Biol* 41.11 (Nov. 1, 1996), URL: http://niremf.ifac.cnr.it/tissprop/ (cited on p. 3).

[24] **Jonasz** Miroslaw. "Absorption coefficient of water: data sources," *Topics in Particle and Dispersion Science* (2007), URL: http://www.tpdsci.com/Tpc/AbsCfOfWaterDat.php (visited on 06/16/2013) (cited on p. 3).

[25] **Strong** Steven P., Roland Koberle, Robert R. de Ruyter van Steveninck, and William Bialek. "Entropy and information in neural spike trains," *Physical Review Letters* 80 (Jan. 5, 1998), 197–200, DOI: 10.1103/PhysRevLett.80.197 (cited on p. 4).

[26] **Wolf** Patrick D. *Thermal Considerations for the Design of an Implanted Cortical Brain–Machine Interface (BMI) In: Reichert WM, editor. Indwelling Neural Implants: Strategies for Contending with the In Vivo Environment.* Boca Raton (FL): CRC Press, 2008, URL: http://www.ncbi.nlm.nih.gov/books/NBK3932/ (cited on pp. 4, 5).

[27] **Sotero** Roberto C. and Yasser Iturria-Medina. "From blood oxygenation level dependent (BOLD) signals to brain temperature maps," *Bulletin of Mathematical Biology* 73.11 (Nov. 2011), 2731–47, DOI: 10.1007/s11538-011-9645-5 (cited on p. 4).

[28] **Lazzi** Gianluca. "Thermal effects of bioimplants," *Engineering in Medicine and Biology Magazine, IEEE* 24.5 (2005), 75–81, ISSN: 0739-5175, DOI: 10.1109/MEMB.2005.1511503 (cited on pp. 4, 5).

[29] **Polderman** Kees H. "Application of therapeutic hypothermia in the icu: opportunities and pitfalls of a promising treatment modality. part 1: indications and evidence," *Intensive Care Medicine* 30.4 (Apr. 1, 2004), DOI: 10.1007/s00134-003-2152-x (cited on p. 4).

[30] *IEC 60825*, Safety of laser products, *Equipment classification and requirements*, 2nd ed., Geneva, Switzerland: International Electrotechnical Commission, Mar. 30, 2007 (cited on p. 5).

[31] **Shapiro** Mikhail G., Kazuaki Homma, Sebastian Villarreal, Claus-Peter Richter, and Francisco Bezanilla. "Infrared light excites cells by changing their electrical capacitance," *Nature Communications* 3.736 (Mar. 13, 2012), DOI: 10.1038/ncomms1742 (cited on p. 5).

[32] **Shapiro** Mikhail G., Michael F. Priest, Peter H. Siegel, and Francisco Bezanilla. "Temperature-mediated effects of millimeter wave stimulation on membrane protein function," *Biophysical Journal* 104.2 (Jan. 2013), 679a, DOI: 10.1016/j.bpj.2012.11.3747 (cited on p. 5).

[33] **Rizk** Michael, Chad A Bossetti, Thomas A Jochum, Stephen H Callender, Miguel AL Nicolelis, et al. "A fully implantable 96-channel neural data acquisition system," *Journal of Neural Engineering* 6.2 (2009), 6002 (cited on p. 5).

[34] **Blinder** Pablo, Philbert S Tsai, John P Kaufhold, Per M Knutsen, Harry Suhl, and David Kleinfeld. "The cortical angiome: an interconnected vascular network with noncolumnar patterns of blood flow," *Nature Neuroscience* (June 9, 2013), DOI: 10.1038/nn.3426 (cited on p. 5).

[35] **Ribeiro** Sidarta, Damien Gervasoni, Ernesto S Soares, Yi Zhou, Shih-Chieh Lin, et al. "Long-lasting novelty-induced neuronal reverberation during slow-wave sleep in multiple forebrain areas," *PLoS Biol* 2.1 (Jan. 2004), e24, DOI: 10.1371/journal.pbio.0020024 (cited on p. 5).

[36] **Nicolelis** Miguel A. L., Dragan Dimitrov, Jose M. Carmena, Roy Crist, Gary Lehew, et al. "Chronic, multisite, multielectrode recordings in macaque monkeys," *Proceedings of the National Academy of Sciences* 100.19 (2003), 11041–6, DOI: 10.1073/pnas.1934665100 (cited on p. 5).

[37] **Pedreira** Carlos, Juan Martinez, Matias J. Ison, and Rodrigo Quian Quiroga. "How many neurons can we see with current spike sorting algorithms?" *Journal of Neuroscience Methods* 211.1 (Oct. 2012), 58–65, DOI: 10/mvv (cited on p. 7).

[38] **Sahani** Maneesh. "Latent variable models for neural data analysis," PhD dissertation, California Institute of Technology, May 14, 1999, URL: http://www.gatsby.ucl.ac.uk/~maneesh/thesis/thesis.double.pdf (visited on 06/16/2013) (cited on p. 7).

[39] **Camuñas-Mesa** Luis A. and Rodrigo Quian Quiroga. "A detailed and fast model of extracellular recordings," *Neural Computation* 25.5 (May 2013), 1191–212, DOI: 10.1162/NECO_a_00433 (cited on p. 7).

[40] **Segev** Ronen, Joe Goodhouse, Jason Puchalla, and Michael J. Berry II. "Recording spikes from a large fraction of the ganglion cells in a retinal patch," *Nature Neuroscience* 7.10 (Oct. 2004), 1155–62, DOI: 10.1038/nn1323 (cited on p. 7).

[41] **Gray** Charles M., Pedro E. Maldonado, Matthew Wilson, and Bruce McNaughton. "Tetrodes markedly improve the reliability and yield of multiple single-unit isolation from multi-unit recordings in cat striate cortex," *Journal of Neuroscience Methods* 63.1–2 (Dec. 1995), 43–54, DOI: 10/ddmxdh (cited on p. 7).

[42] **Gold** Carl, Darrell A. Henze, and Christof Koch. "Using extracellular action potential recordings to constrain compartmental models," *Journal of Computational Neuroscience* 23 (Aug. 23, 2007), 39–58, DOI: 10.1007/s10827-006-0018-2 (cited on p. 7).

[43] **Du** Jiangang, Timothy J. Blanche, Reid R. Harrison, Henry A. Lester, and Sotiris C. Masmanidis. "Multiplexed, high density electrophysiology with nanofabricated neural probes," *PLoS ONE* 6.10 (Oct. 12, 2011), e26204, DOI: 10.1371/journal.pone.0026204 (cited on pp. 7, 8).

[44] **Henze** Darrell A., Zsolt Borhegyi, Jozsef Csicsvari, Akira Mamiya, Kenneth D. Harris, and György Buzsáki. "Intracellular features predicted by extracellular recordings in the hippocampus in vivo," *Journal of Neurophysiology* 84.1 (2000), 390–400, eprint: http://jn.physiology.org/content/84/1/390.full.pdf+html (cited on p. 7).

[45] **Buzsáki** György. "Large-scale recording of neuronal ensembles," *Nature Neuroscience* 7 (5 May 2004), DOI: 10.1038/nn1233 (cited on p. 7).

[46] **Wessberg** Johan, Christopher R. Stambaugh, Jerald D. Kralik, Pamela D. Beck, Mark Laubach, et al. "Real-time prediction of hand trajectory by ensembles of cortical neurons in primates," *Nature* 408 (6810 Nov. 16, 2000), DOI: 10.1038/35042582 (cited on p. 7).

[47] **Carmena** Jose M, Mikhail A Lebedev, Roy E Crist, Joseph E O'Doherty, David M Santucci, et al. "Learning to control a brain-machine interface for reaching and grasping by primates," *PLoS Biol* 1.2 (Oct. 2003), e42, DOI: 10.1371/journal.pbio.0000042 (cited on p. 7).

[48] **Koralek** Aaron C., Xin Jin, John D. Long II, Rui M. Costa, and Jose M. Carmena. "Corticostriatal plasticity is necessary for learning intentional neuroprosthetic skills," *Nature* 483 (7389 Mar. 15, 2012), DOI: 10.1038/nature10845 (cited on p. 7).

[49] **Jin** Xin and Rui M. Costa. "Start/stop signals emerge in nigrostriatal circuits during sequence learning," *Nature* 466 (7305 July 22, 2010), DOI: 10.1038/nature09263 (cited on p. 7).

[50] **Llinás** Rodolfo R., Kerry D. Walton, Masayuki Nakao, Ian Hunter, and Patrick A. Anquetil. "Neuro-vascular central nervous recording/stimulating system: Using nanotechnology probes," *Journal of Nanoparticle Research* 7.2–3 (June 2005), 111–27, DOI: 10.1007/s11051-005-3134-4 (cited on p. 8).

[51] **Schmidt** Richard F. and Gerhard Thews, eds. *Human Physiology*, 2nd ed., New York: Springer-Verlag, Sept. 1989, URL: http://www.amazon.com/dp/0387194320/ (cited on p. 8).

[52] **Loffredo** Francesco and Richard T. Lee. "Therapeutic vasculogenesis: It takes two," *Circulation Research* 103.2 (July 18, 2008), 128–30, DOI: 10.1161/CIRCRESAHA.108.180604 (cited on p. 8).

[53] **Jadhav** Amol D., Ivan Aimo, Daniel Cohen, Peter Ledochowitsch, and Michel M. Maharbiz. "Cyborg eyes: Microfabricated neural interfaces implanted during the development of insect sensory organs produce stable neurorecordings in the adult," *Micro Electro Mechanical Systems*, IEEE 25th International Conference on, IEEE MEMS 2012 (Paris), Jan. 29–Feb. 2, 2012, 937–40, DOI: 10.1109/MEMSYS.2012.6170340 (cited on p. 8).

[54] **Jensen** Winnie, Ulrich G. Hofmann, and Ken Yoshida. "Assessment of subdural insertion force of single-tine microelectrodes in rat cerebral cortex," *Engineering in Medicine and Biology Society*, Proceedings of the 25th Annual International Conference of the IEEE, EMBC'03 (Cancun, Mexico), vol. 3, Sept. 17–21, 2003, 2168–71, DOI: 10.1109/IEMBS.2003.1280170 (cited on p. 8).

[55] **Najafi** Khalil and Jamille F. Hetke. "Strength characterization of silicon microprobes in neurophysiological tissues," *IEEE Transactions on Biomedical Engineering* 37.5 (May 1990), 474–81, DOI: 10.1109/10.55638 (cited on p. 8).

[56] **Weibel** Douglas B., Piotr Garstecki, Declan Ryan, Willow R. DiLuzio, Michael Mayer, et al. "Microoxen: Microorganisms to move microscale loads," *Proceedings of the National Academy of Sciences of the United States of America* 102.34 (2005), 11963–7, DOI: 10.1073/pnas.0505481102 (cited on p. 8).

[57] **Kodandaramaiah** Suhasa B, Giovanni Talei Franzesi, Brian Y Chow, Edward S Boyden, and Craig R Forest. "Automated whole-cell patch-clamp electrophysiology of neurons in vivo," *Nature Methods* 9 (6), DOI: 10.1038/nmeth.1993 (cited on p. 9).

[58] **Smetters** Diana, Ania Majewska, and Rafael Yuste. "Detecting action potentials in neuronal populations with calcium imaging," *METHODS: A Companion to Methods in Enzymology* 18 (2 June 1999), DOI: 10.1006/meth.1999.0774 (cited on p. 9).

[59] **Barnett** Lauren, Jelena Platisa, Marko Popovic, Vincent A. Pieribone, and Thomas Hughes. "A fluorescent, genetically-encoded voltage probe capable of resolving action potentials," *PLoS ONE* 7.9 (Sept. 2012), e43454, DOI: 10.1371/journal.pone.0043454 (cited on p. 9).

[60] **Kralj** Joel M, Adam D Douglass, Daniel R Hochbaum, Dougal Maclaurin, and Adam E Cohen. "Optical recording of action potentials in mammalian neurons using a microbial rhodopsin," *Nature Methods* 9 (1), DOI: 10.1038/nmeth.1782 (cited on p. 9).

[61] **Storace** Douglas. A., Uhna. Sung, Jelena. Platisa, Lawrence. B. Cohen, and Vincent. A. Pieribone. "In Vivo Imaging of Odor-Evoked Responses in the Olfactory Bulb using Arclight, a Novel Fp Voltage Probe," *Biophysical Journal* 104 (Jan. 2013), 679, DOI: 10.1016/j.bpj.2012.11.3751 (cited on p. 9).

[62] **Kobat** Demirhan, Michael E. Durst, Nozomi Nishimura, Angela W. Wong, Chris B. Schaffer, and Chris Xu. "Deep tissue multiphoton microscopy using longer wavelength excitation," *Optics Express* 17.16 (Aug. 3, 2009), 13354–64, DOI: 10.1364/OE.17.013354 (cited on p. 9).

[63] **Kobat** Demirhan, Nicholas G. Horton, and Chris Xu. "In vivo two-photon microscopy to 1.6-mm depth in mouse cortex," *Journal of Biomedical Optics* 16.10 (2011), DOI: 10.1117/1.3646209 (cited on p. 9).

[64] **Filonov** Grigory S., Kiryi D. Platkevich, Li-Min Ting, Jinghang Zhang, Kami Kim, and Vladislav V. Verkhusha. "Bright and stable near-infrared fluorescent protein for *in vivo* imaging," *Nature Biotechnology* 29.8 (online July 17, 2011), 757–61, DOI: 10.1038/nbt.1918 (cited on p. 9).

[65] **Shcherbakova** Daria M. and Vladislav V. Verkhusha. "Near-infrared fluorescent proteins for multicolor *in vivo* imaging," *Nature Methods* (online June 16, 2013), DOI: 10.1038/nmeth.2521, prepublished (cited on p. 9).

[66] **Shcherbo** Dmitry, Christopher S. Murphy, Galina V. Ermakova, Elena A. Solovieva, Tatiana V. Chepurnykh, et al. "Far-red fluorescent tags for protein imaging in living tissues," *Biochem J* 418.3 (2009), 567–74, DOI: 10.1042/BJ20081949 (cited on p. 9).

[67] **Alivisatos** A. Paul, Anne M. Andrews, Edward S. Boyden, Miyoung Chun, George M. Church, et al. "Nanotools for neuroscience and brain activity mapping," *ACS Nano* 7.3 (Mar. 26, 2013), 1850–66, DOI: 10.1021/nn4012847 (cited on pp. 9, 10).

[68] **Conkey** Donald B., Antonio M. Caravaca-Aguirre, and Rafael Piestun. "High-speed scattering medium characterization with application to focusing light through turbid media," *Optics Express* 20.2 (Jan. 16, 2012), 1733–40, DOI: 10.1364/OE.20.001733 (cited on p. 9).

[69] **Nixon** Micha, Ori Katz, Eran Small, Yaron Bromberg, Asher A. Friesem, et al. "Real-time wavefront-shaping through scattering media by all optical feedback," (Mar. 13, 2013), arXiv:1303.3161 [physics.optics] (cited on p. 9).

[70] **Chaigne** Thomas, Ori Katz, A. Claude Boccara, Mathias Fink, Emmanuel Bossy, and Sylvain Gigan. "Controlling light in scattering media noninvasively using the photo-acoustic transmission-matrix," (May 27, 2013), arXiv:1305.6246 [physics.optics] (cited on p. 9).

[71] **Mahalati** Reza Nasiri, Ruo Yu Gu, and Joseph M. Kahn. "Resolution limits for imaging through multi-mode fiber," *Optics Express* 21.2 (Jan. 28, 2013), 1656–68, DOI: 10.1364/OE.21.001656 (cited on p. 10).

[72] **Zorzos** Anthony N., Edward S. Boyden, and Clifton G. Fonstad. "Multiwaveguide implantable probe for light delivery to sets of distributed brain targets," *Optics Letters* 35.24 (Dec. 15, 2010), 4133–5, DOI: 10.1364/OL.35.004133 (cited on p. 10).

[73] **Zorzos** Anthony N., Jorg Scholvin, Edward S. Boyden, and Clifton G. Fonstad. "Three-dimensional multiwaveguide probe array for light delivery to distributed brain circuits," *Optics Letters* 37.23 (Dec. 1, 2012), 4841–3, DOI: 10.1364/OL.37.004841 (cited on p. 10).

[74] **Wakin** Michael B., Jason N. Laska, Marco F. Duarte, Dror Baron, Shriram Sarvotham, et al. "Compressive imaging for video representation and coding," *Picture Coding Symposium*, Proceedings of the 25th International, PCS'06 (Beijing, China), Apr. 24–26, 2006, URL: http://inside.mines.edu/~mwakin/papers/pcs-camera.pdf (visited on 06/16/2013) (cited on p. 10).

[75] **Studer** Vincent, Jérome Bobin, Makhlad Chahid, Hamed Shams Mousavi, Emmanuel Candes, and Maxime Dahan. "Compressive fluorescence microscopy for biological and hyperspectral imaging," *Proceedings of the National Academy of Sciences of the United States of America* 109.26 (June 26, 2012), E1679–E1687, DOI: 10.1073/pnas.1119511109 (cited on p. 10).

[76] **Tian** Nian, Qingchun Guo, Anle Wang, Dongli Xu, and Ling Fu. "Fluorescence ghost imaging with pseudothermal light," *Optics Letters* 36.16 (Aug. 15, 2011), 3302–4, DOI: 10.1364/OL.36.003302 (cited on p. 10).

[77] **Sun** Baoqing, Matthew P. Edgar, Richard Bowman, Liberty E. Vittert, Stuart Welsh, et al. "3D computational imaging with single-pixel detectors," *Science* 340.6134 (May 17, 2013), 844–7, DOI: 10.1126/science.1234454 (cited on p. 10).

[78] **Huang** Gang, Hong Jiang, Kim Matthews, and Paul Wilford. "Lensless imaging by compressive sensing," *International Conference on Image Processing*, Proceedings of the 20th IEEE, ICIP 2013 (Melbourne, Australia), Sept. 15–18, 2013, forthcoming (cited on p. 10).

[79] **Murray** Teresa A. and Michael J. Levene. "Singlet gradient index lens for deep in vivo multiphoton microscopy," *Journal of Biomedical Optics* 17.2 (Mar. 2, 2012), 021106, DOI: 10/mvt (cited on p. 10).

[80] **Kang** Jeon Woong, Pilhan Kim, Carlo Amadeo Alonzo, Hyunsung Park, and Seok H. Yun. "Two-photon microscopy by wavelength-swept pulses delivered through single-mode fiber," *Optics Letters* 35.2 (Jan. 15, 2010), 181–3, DOI: 10.1364/OL.35.000181 (cited on p. 10).

[81] **Flusberg** Benjamin A., Eric D. Cocker, Wibool Piyawattanametha, Jürgen C. Jung, Eunice L. M. Cheung, and Mark J. Schnitzer. "Fiber-optic fluorescence imaging," *Nature Methods* 2.12 (online Nov. 18, 2005), 941–50, DOI: 10.1038/nmeth820 (cited on p. 10).

[82] **Wang** Ying Min, Benjamin Judkewitz, Charles A. DiMarzio, and Changhuei Yang. "Deep-tissue focal fluorescence imaging with digitally time-reversed ultrasound-encoded light," *Nature Communications* 3.928 (June 26, 2012), DOI: 10.1038/ncomms1925 (cited on pp. 10, 24).

[83] **Mahan** Gerald D., William E. Engler, Jerome J. Tiemann, and Egidijus E. Uzgiris. "Ultrasonic tagging of light: Theory," *Proceedings of the National Academy of Sciences of the United States of America* 95.24 (Nov. 24, 1998), 14015–9, DOI: 10.1073/pnas.95.24.14015 (cited on p. 10).

[84] **Vučinić** Dejan and Terrence J. Sejnowski. "A compact multiphoton 3d imaging system for recording fast neuronal activity," *PLoS ONE* 2.8 (Aug. 8, 2007), e699, DOI: 10.1371/journal.pone.0000699 (cited on p. 10).

[85] **Striker** George, Vinod Subramaniam, Claus A. M. Seidel, and Andreas Volkmer. "Photochromicity and fluorescence lifetimes of green fluorescent protein," *The Journal of Physical Chemistry B* 103.40 (Oct. 7, 1999), 8612–7, DOI: 10.1021/jp991425e (cited on p. 10).

[86] **Wilt** Brian A., James E. Fitzgerald, and Mark J. Schnitzer. "Photon shot noise limits on optical detection of neuronal spikes and estimation of spike timing," *Biophysical Journal* 104.1 (Jan. 8, 2013), 51–62, DOI: 10.1016/j.bpj.2012.07.058 (cited on p. 10).

[87] **Kim** Ki Hean, Christof Buehler, and Peter T. C. So. "High-speed, two-photon scanning microscope," *Applied Optics* 38.28 (Oct. 1, 1999), 6004–9, DOI: 10.1364/AO.38.006004 (cited on pp. 10, 11).

[88] **Wilson** Jennifer M., Daniel A. Dombeck, Manuel Díaz-Ríos, Ronald M. Harris-Warrick, and Robert M. Brownstone. "Two-photon calcium imaging of network activity in XFP-expressing neurons in the mouse," *Journal of Neurophysiology* 97.4 (Apr. 2007), 3118–25, DOI: 10.1152/jn.01207.2006 (cited on p. 10).

[89] **Masters** Barry R. *Confocal Microscopy and Multiphoton Excitation Microscopy: The Genesis of Live Cell Imaging*, SPIE Press Monograph PM161, Bellingham, WA, USA: SPIE Publications, Feb. 9, 2006, ISBN: 9780819461186, URL: http://spie.org/x648.html?product_id=660403 (cited on p. 11).

[90] **Drobizhev** Mikhail, Nikolay S Makarov, Shane E Tillo, Thomas E Hughes, and Aleksander Rebane. "Two-photon absorption properties of fluorescent proteins," *Nature methods* 8.5 (2011), 393–9 (cited on p. 11).

[91] **Goeppert-Mayer** Maria. "Elementary processes with two quantum transitions," *Annalen der Physik* 18.7-8 (), ISSN: 1521-3889, DOI: 10.1002/andp.200910358, URL: http://dx.doi.org/10.1002/andp.200910358 (cited on p. 11).

[92] **Seliger** Howard H. and William D. McElroy. "Spectral emission and quantum yield of firefly bioluminescence," *Archives of Biochemistry and Biophysics* 88.1 (May 1960), 136–41, DOI: 10/d2v3gx (cited on p. 11).

[93] **Molter** Timothy W., Sarah C. McQuaide, Martin T. Suchorolski, Tim J. Strovad, Lloyd W. Burgess, et al. "A microwell array device capable of measuring single-cell oxygen consumption rates," *Sensors and Actuators B: Chemical* 135.2 (Jan. 15, 2009), 678–86, DOI: 10.1016/j.snb.2008.10.036 (cited on p. 11).

[94] **Blanchard** Romain, Svetlana V. Boriskina, Patrice Genevet, Mikhail A. Kats, Jean-Philippe Tetienne, et al. "Multi-wavelength mid-infrared plasmonic antennas with single nanoscale focal point," *Optics Express* 19.22 (Oct. 24, 2011), 22113–24, DOI: 10.1364/OE.19.022113 (cited on p. 11).

[95] **Widder** Edith A., Michael I. Latz, Peter J. Herring, and James F. Case. "Far red bioluminescence from two deep-sea fishes," *Science* 225.4661 (Aug. 3, 1984), 512–4, DOI: 10.1126/science.225.4661.512 (cited on p. 12).

[96] **Campbell** Anthony K. and Peter J. Herring. "A novel red fluorescent protein from the deep sea luminous fish *Malacosteus niger*," *Comparative Biochemistry and Physiology Part B: Comparative Biochemistry* 86B.2 (1987), 411–7, DOI: 10/cz84np (cited on p. 12).

[97] **Livet** Jean, Tamily A. Weissman, Hyuno Kang, Ryan W. Draft, Ju Lu, et al. "Transgenic strategies for combinatorial expression of fluorescent proteins in the nervous system," *Nature* 450 (Nov. 1, 2007), 56–62, DOI: 10.1038/nature06293 (cited on p. 12).

[98] **Usami** Mitsuo, Hisao Tanabe, Akira Sato, Isao Sakama, Yukio Maki, et al. "A 0.05×0.05 mm^2 RFID chip with easily scaled-down ID-memory," *International Solid-State Circuits Conference, 2007 IEEE*, Digest of Technical Papers, ISSCC 2007 (San Francisco, CA, USA), Feb. 11–15, 2007, 482–3, DOI: 10.1109/ISSCC.2007.373504 (cited on p. 12).

[99] *Monza 5 Tag Chip datasheet*, Impinj, Inc., Seattle, WA, USA, Feb. 14, 2012, URL: http://www.impinj.com/Documents/Tag_Chips/Monza_5_Datasheet (visited on 06/20/2013) (cited on p. 12).

[100] **Biederman** William, Daniel J. Yaeger, Nathan Narevsky, Aaron C. Koralek, Jose M. Carmena, et al. "A fully-integrated, miniaturized (0.125 mm^2) 10.5 μW wireless neural sensor," *IEEE Journal of Solid-State Circuits* 48.4 (Apr. 2013), 960–70, DOI: 10.1109/JSSC.2013.2238994 (cited on p. 12).

[101] **Cannon** Gregory J. and Joel A. Swanson. "The macrophage capacity for phagocytosis," *Journal of Cell Science* 101 (Apr. 1, 1992), 907–13, URL: http://jcs.biologists.org/content/101/4/907 (cited on p. 12).

[102] **Kadiu** Irena, Ari Nowacek, Joellyn McMillan, and Howard E. Gendelman. "Macrophage endocytic trafficking of antiretroviral nanoparticles," *Nanomedicine* 6.6 (Mar. 27, 2011), DOI: 10.2217/nnm.11.27 (cited on p. 12).

[103] **Bennett** Charles H. "Logical reversibility of computation," *IBM Journal of Research and Development* 17.6 (Nov. 1973), 525–32, DOI: 10.1147/rd.176.0525 (cited on p. 12).

[104] **Landauer** Rolf W. "Irreversibility and heat generation in the computing process," *IBM Journal of Research and Development* 5.3 (July 1961), 183–91, DOI: 10.1147/rd.53.0183 (cited on p. 12).

[105] **Yablonovitch** Eli. *Replacing the transistor: searching for the milli-volt switch*, Hong Kong University of Science and Technology, Nov. 21, 2011, URL: http://ustlib.ust.hk/record=b1161099 (cited on pp. 12, 13).

[106] **Steyaert** Michel S. J., Willy M. C. Sansen, and Zhong-Yuan Chang. "A micropower low-noise monolithic instrumentation amplifier for medical purposes," *IEEE Journal of Solid-State Circuits* 22.6 (Dec. 1987), 1163–8, DOI: 10.1109/JSSC.1987.1052869 (cited on p. 13).

[107] **Tucker** Rodney S. and Kerry Hinton. "Energy consumption and energy density in optical and electronic signal processing," *IEEE Photonics Journal* 3.5 (Oct. 2011), 821–33, DOI: 10.1109/JPHOT.2011.2166254 (cited on pp. 13, 14).

[108] **Koomey** Jonathan G., Stephen Berard, Marla Sanchez, and Henry Wong. "Implications of historical trends in the electrical efficiency of computing," *IEEE Annals of the History of Computing* 33.3 (Mar. 2011), 46–54, DOI: 10.1109/MAHC.2010.28 (cited on p. 13).

[109] **Tucker** Rodney S. "Green optical communications — Part II: Energy limitations in networks," *IEEE Journal of Selected Topics in Quantum Electronics* 17.2 (Apr. 7, 2011), 261–74, DOI: 10.1109/JSTQE.2010.2051217 (cited on p. 13).

[110] *UHF / Microwave RFID Transponder ASIC IPMS_MWST1*, Datasheet, Fraunhofer Institute for Photonic Microsystems, Nov. 7, 2011, URL: http://www.ipms.fraunhofer.de/content/dam/ipms/common/products/WMS/Transponder/uhf-transponder-e.pdf (visited on 06/16/2013) (cited on p. 13).

[111] **Sarpeshkar** Rahul. "Analog versus digital: extrapolating from electronics to neurobiology," *Neural Computation* 10.7 (Oct. 1, 1998), 1601–38, DOI: 10/fvhwq3 (cited on p. 13).

[112] **Rapoport** Benjamin I., Woradorn Wattanapanitch, Héctor Luis Penagos Vargas, Sam Musallam, Richard A. Andersen, and Rahul Sarpeshkar. "A biomimetic adaptive algorithm and low-power architecture for implantable neural decoders," *Engineering in Medicine and Biology Society*, Annual International Conference of the IEEE, EMBC 2009 (Minneapolis, MN, USA), Sept. 3–6, 2009, 4214–7, DOI: 10.1109/IEMBS.2009.5333793 (cited on p. 13).

[113] **Mandal** Soumyajit and Rahul Sarpeshkar. "Low-power CMOS rectifier design for RFID applications," *IEEE Transactions on Circuits and Systems I: Regular Papers* 54.6 (June 11, 2007), 1177–88, DOI: 10.1109/TCSI.2007.895229 (cited on pp. 13, 15).

[114] **Sun** Young-Ho and Kai Chang. "A high-efficiency dual-frequency rectenna for 2.45- and 5.8-GHz wireless power transmission," *IEEE Transactions on Microwave Theory and Techniques* 50.7 (July 2002), 1784–9, DOI: 10.1109/TMTT.2002.800430 (cited on p. 15).

[115] **Ionescu** Adrian M. and Heike Riel. "Tunnel field-effect transistors as energy-efficient electronic switches," *Nature* 479 (Nov. 17, 2011), 329–37, DOI: 10.1038/nature10679 (cited on p. 15).

[116] **Liu** Tsu-Jae King, Dejan Marković, Vladimir Stojanović, and Elad Alon. "The relay reborn," *IEEE Spectrum* 49.4 (Apr. 2012), 40–3, DOI: 10.1109/MSPEC.2012.6172808 (cited on p. 15).

[117] **Ozeri** Shaul and Doron Shmilovitz. "Ultrasonic transcutaneous energy transfer for powering implanted devices," *Ultrasonics* 50.6 (May 2010), 556–66, DOI: 10.1016/j.ultras.2009.11.004 (cited on p. 15).

[118] **Gershenfeld** Neil. *The physics of information technology*, Cambridge University Press, 2000 (cited on p. 15).

[119] **Kitagawa** Yutaro, Yuji Hiraoka, Takashi Honda, Taishi Ishikura, Hiroyuki Nakamura, and Tsuyoshi Kimura. "Low-field magnetoelectric effect at room temperature," *Nature Materials* 10 (2010), 797–802, DOI: 10.1038/nmat2826 (cited on p. 15).

[120] **Priya** Shashank, Jungho Ryu, Chee-Sung Park, Josiah Oliver, Jong-Jin Choi, and Dong-Soo Park. "Piezoelectric and magnetoelectric thick films for fabricating power sources in wireless sensor nodes," *Sensors* 9.8 (2009), DOI: 10.3390/s90806362 (cited on p. 15).

[121] **Yue** Kun, Rakesh Guduru, HongJeongmin, Ping Liang, Madhavan Nair, and Sakhrat Khizroev. "Magneto-electric nano-particles for non-invasive brain stimulation," *PLoS ONE* 7.9 (Sept. 2012), e44040, DOI: 10.1371/journal.pone.0044040 (cited on p. 15).

[122] **Fiebig** Manfred. "Revival of the magnetoelectric effect," *Journal of Physics D: Applied Physics* 38.8 (2005), R123, URL: http://stacks.iop.org/0022-3727/38/i=8/a=R01 (cited on p. 15).

[123] **Karalis** Aristeidis, J.D. Joannopoulos, and Marin Soljačić. "Efficient wireless non-radiative mid-range energy transfer," *Annals of Physics* 323.1 (2008), 34 –48, ISSN: 0003-4916, DOI: http://dx.doi.org/10.1016/j.aop.2007.04.017 (cited on p. 15).

[124] **Ho** J.S., Sanghoek Kim, and A.S.Y. Poon. "Midfield wireless powering for implantable systems," *Proceedings of the IEEE* 101.6 (2013), 1369–78, ISSN: 0018-9219, DOI: 10.1109/JPROC.2013.2251851 (cited on p. 15).

[125] **Bett** Andreas W., Frank Dimroth, Rüdiger Löckenhoff, Eduard Oliva, and Johannes Schubert. "III-V solar cells under monochromatic illumination," *Photovoltaic Specialists Conference, 2008*, Proceedings of the 33rd IEEE, PVSC'08 (San Diego, CA, USA), May 11–16, 2008, 1–5, DOI: 10.1109/PVSC.2008.4922910 (cited on p. 15).

[126] **Safari** Ahmad and E. Koray Akdoğan, eds. *Piezoelectric and Acoustic Materials for Transducer Applications*, Boston, MA, USA: Springer, 2008, URL: http://www.amazon.com/dp/0387765387 (cited on p. 15).

[127] **Xu** Tian-Bing, Emilie J. Siochi, Jin Ho Kang, Lei Zuo, Wanlu Zhou, et al. "Energy harvesting using a PZT ceramic multilayer stack," *Smart Materials and Structures* 22 (Apr. 2013), 065015, DOI: 10/mvs (cited on p. 15).

[128] **Krimholtz** Richard S., David A. Leedom, and George L. Matthaei. "New equivalent circuits for elementary piezoelectric transducers," *Electronics Letters* 6.13 (June 25, 1970), 398–9, DOI: 10.1049/el:19700280 (cited on p. 15).

[129] **Castillo** Martha, Pedro Acevedo, and Eduardo Moreno. "KLM model for lossy piezoelectric transducers," *Ultrasonics* 41.8 (Nov. 2003), 671–9, DOI: 10/b4hpcw (cited on p. 15).

[130] **Rapoport** Benjamin I., Jakub T. Kedzierski, and Rahul Sarpeshkar. "A glucose fuel cell for implantable brain-machine interfaces," *PLoS ONE* 7.6 (June 12, 2012), e38436, DOI: 10.1371/journal.pone.0038436 (cited on pp. 15, 16).

[131] **Silver** Ian A. and Maria Erecińska.
"Extracellular glucose concentration in mammalian brain: continuous monitoring of changes during increased neuronal activity and upon limitation in oxygen supply in normo-, hypo-, and hyperglycemic animals,"
The Journal of Neuroscience 14.8 (Aug. 1994), 5068–76, URL: http://www.jneurosci.org/content/14/8/5068.long (cited on p. 15).

[132] **Ivanov** Kirill P., M. K. Kalinina, and Yu I. Levkovich.
"Blood flow velocity in capillaries of brain and muscles and its physiological significance,"
Microvascular Research 22.2 (Sept. 1981), 143–55, DOI: 10/cc8sqk (cited on p. 15).

[133] **Cho** Namjun, Seong-Jun Song, Sunyoung Kim, Shiho Kim, and Hoi-Jun Yoo.
"A 5.1-μw UHF RFID tag chip integrated with sensors for wireless environmental monitoring,"
Solid-State Circuits Conference, 2005, Proceedings of the 31st European, ESSCIRC 2005 (Grenoble, France), Sept. 12–16, 2005, 279–82, DOI: 10.1109/ESSCIR.2005.1541614 (cited on p. 16).

[134] **Cover** Thomas M. and Joy A. Thomas. *Elements of Information Theory*, 2nd ed.,
Wiley Series in Telecommunications and Signal Processing, Hoboken, NJ: Wiley-Interscience, July 18, 2006, URL: http://www.amazon.com/dp/0471241954 (cited on p. 16).

[135] **Carp** Stefan A., Nadàege Roche-Labarbe, Maria-Angela Franceschini, Vivek J. Srinivasan, Sava Sakadžić, and David A. Boas. "Due to intravascular multiple sequential scattering, diffuse correlation spectroscopy of tissue primarily measures relative red blood cell motion within vessels," *Biomedical Optics Express* 2.7 (June 24, 2011), 2047–54, DOI: 10.1364/BOE.2.002047 (cited on p. 18).

[136] **Tulino** Antonia M. and Sergio Verdú. "Random matrix theory and wireless communications,"
Foundations and Trends in Communications and Information Theory 1.1 (June 28, 2004), 1–182, DOI: 10.1561/0100000001 (cited on p. 18).

[137] **Shiu** Da-shan, Gerard J. Foschini, Michael J. Gans, and Joseph M. Kahn.
"Fading correlation and its effect on the capacity of multielement antenna systems,"
IEEE Transactions on Communications 48.3 (Mar. 2000), 502–13, DOI: 10.1109/26.837052 (cited on p. 18).

[138] **Spencer** Quentin H., Christian B. Peel, A. Lee Swindlehurst, and Martin Haardt.
"An introduction to the multi-user MIMO downlink," *IEEE Communications Magazine* 42.10 (Oct. 2004), 60–7, DOI: 10.1109/MCOM.2004.1341262 (cited on p. 18).

[139] **Moustakas** Aris L., Harold U. Baranger, Leon Balents, Anirvan Sengupta, and Steven H. Simon.
"Communication through a diffusive medium: Coherence and capacity," *Science* 287.5451 (Jan. 14, 2000), 287–90, DOI: 10.1126/science.287.5451.287 (cited on p. 18).

[140] **Popoff** Sebastien M., Geoffroy Lerosey, Rémi Carminati, Mathias Fink, A. Claude Boccara, and Sylvain Gigan.
"Measuring the transmission matrix in optics: An approach to the study and control of light propagation in disordered media," *Physical Review Letters* 104.10 (Mar. 12, 2010), e100601, DOI: 10.1103/PhysRevLett.104.100601 (cited on p. 18).

[141] **Berkovits** Richard. "Sensitivity of the multiple-scattering speckle pattern to the motion of a single scatterer,"
Physical Review B 43.10 (Apr. 1, 1991), 8638–40, DOI: 10.1103/PhysRevB.43.8638 (cited on pp. 18, 20).

[142] **Derode** Arnaud, Arnaud Tourin, Julien de Rosny, Mickaël Tanter, Sylvain Yon, and Mathias Fink.
"Taking advantage of multiple scattering to communicate with time-reversal antennas,"
Physical Review Letters 90.1 (Jan. 10, 2003), e014301, DOI: 10.1103/PhysRevLett.90.014301 (cited on p. 19).

[143] **Bakopoulos** Paraskevas, Irene S. Karanasiou, Nikos Pleros, Panagiotis Zakynthinos, Nikolaos Uzunoglu, and Hercules Avramopoulos.
"A tunable continuous wave (CW) and short-pulse optical source for THz brain imaging applications,"
Measurement Science and Technology 20 (Sept. 4, 2009), e104001, DOI: 10/dw7hhz (cited on p. 19).

[144] **Tonouchi** Masayoshi. "Cutting-edge terahertz technology," *Nature Photonics* 1 (Feb. 2007), 97–105, DOI: 10.1038/nphoton.2007.3 (cited on p. 19).

[145] **Hoskins** Peter R., Kevin Martin, and Abigail Thrush, eds. *Diagnostic Ultrasound: Physics and Equipment*, 2nd ed.,
New York: Cambridge University Press, July 26, 2010, URL: http://www.amazon.com/dp/052175710X (cited on p. 19).

[146] **Foster** F. Stuart, Charles J. Pavlin, Kasia A. Harasiewicz, Donald A. Christopher, and Daniel H. Turnbull.
"Advances in ultrasound biomicroscopy," *Ultrasound in Medicine & Biology* 26.1 (Jan. 2000), 1–27, DOI: 10/fmzgkm (cited on p. 19).

[147] **Gómez-Martínez** Rodrigo, Patricia Vázquez, Marta Duch, Alejandro Muriano, Daniel Pinacho, et al.
"Intracellular silicon chips in living cells," *Small* 6.4 (Feb. 22, 2010), 499–502, DOI: 10.1002/smll.200901041 (cited on p. 19).

[148] **Dyson** Freeman. "'Radiotelepathy', the direct communication of feelings and thought from brain to brain," *What Will Change Everything?* The *Edge* Annual Question, ed. by **Brockman** John, *Edge*.org, Jan. 2009, URL: http://www.edge.org/q2009/q09_3.html#dyson (cited on p. 19).

[149] **Bush** Stephen F. "Toward in vivo nanoscale communication networks: utilizing an active network architecture," *Front. Comput. Sci China* 5.3 (Sept. 2011), 316–26, ISSN: 1673-7350, DOI: 10.1007/s11704-011-0116-9, URL: http://dx.doi.org/10.1007/s11704-011-0116-9 (cited on p. 20).

[150] **Mohr** Peter J., Barry N. Taylor, and David B. Newell. "CODATA recommended values of the fundamental physical constants: 2010," *Reviews of Modern Physics* 84.4 (Nov. 13, 2012), 1527–605, DOI: 10.1103/RevModPhys.84.1527 (cited on p. 20).

[151] **Rooney** William D., Glyn Johnson, Xin Li, Eric R. Cohen, Seong-Gi Kim, et al. "Magnetic field and tissue dependencies of human brain longitudinal ^1H_2O relaxation in vivo," *Magnetic Resonance in Medicine* 57.2 (Feb. 2007), 308–18, DOI: 10.1002/mrm.21122 (cited on p. 20).

[152] **Deichmann** Ralf, Holger Adolf, Ulrich Nöth, Sean P. Morrissey, Christian Schwarzbauer, and Axel Haase. "Fast T_2-mapping with SNAPSHOT FLASH imaging," *Magnetic Resonance Imaging* 13.4 (1995), 633–9, DOI: 10/bpj92v (cited on p. 20).

[153] **Shapiro** Mikhail G., Gil G. Westmeyer, Philip A. Romero, Jerzy O. Szablowski, Benedict Küster, et al. "Directed evolution of a magnetic resonance imaging contrast agent for noninvasive imaging of dopamine," *Nature Biotechnology* 28.3 (Mar. 2010), 264–70, DOI: 10.1038/nbt.1609 (cited on pp. 20, 22).

[154] **Koretsky** Alan P. "Is there a path beyond BOLD? Molecular imaging of brain function," *NeuroImage* 62.2 (Aug. 15, 2012), 1208–15, DOI: 10/mvr (cited on p. 20).

[155] **Hsieh** Vivian and Alan Jasanoff. "Bioengineered probes for molecular magnetic resonance imaging in the nervous system," *ACS Chemical Neuroscience* 3.8 (online July 11, 2012), 593–602, DOI: 10.1021/cn300059r (cited on p. 20).

[156] **Stehling** Michael K., Robert Turner, and Peter Mansfield, *Science* 254.5028 (Oct. 4, 1991), 43–50, DOI: 10.1126/science.1925560 (cited on p. 20).

[157] **Haase** Axel, Jens Frahm, Dieter Matthaei, Wolfgang Hänicke, and Klaus-Dietmar Merboldt. "FLASH imaging: Rapid NMR imaging using low flip-angle pulses," *Journal of Magnetic Resonance* 67.2 (Apr. 1986), 258–66, DOI: 10/cz8k2n (cited on p. 20).

[158] **Wiesinger** Florian, Pierre-François Van de Moortele, Gregor Adriany, Nicola De Zanche, Kamil Ugurbil, and Klaas P. Prüssman. "Potential and feasibility of parallel MRI at high field," *NMR in Biomedicine* 19 (2006), 368–78, DOI: 10.1002/nbm.1050 (cited on p. 20).

[159] **Glover** Paul and Sir Peter Mansfield. "Limits to magnetic resonance microscopy," *Reports on Progress in Physics* 65.10 (Oct. 2002), DOI: 10/cv63tt (cited on pp. 20, 21).

[160] **Yu** Xin, Daniel Glen, Shumin Wang, Stephen Dodd, Yoshiyuki Hirano, et al. "Direct imaging of macrovascular and microvascular contributions to BOLD fMRI in layers IV–V of the rat whisker-barrel cortex," *NeuroImage* 59.2 (Jan. 16, 2012), 1451–60, DOI: 10/ff6cts (cited on p. 21).

[161] **Null** Brian, Corey W. Liu, Maj Hedehus, Steven Conolly, and Ronald W. Davis. "High-resolution, *in vivo* magnetic resonance imaging of *Drosophila* at 18.8 tesla," *PLoS ONE* 3.7 (July 30, 2008), e2817, DOI: 10.1371/journal.pone.0002817 (cited on p. 21).

[162] **Zhang** Shuo, Kai Tobias Block, and Jens Frahm. "Magnetic resonance imaging in real time: Advances using radial FLASH," *Journal of Magnetic Resonance Imaging* 31.1 (Jan. 2010), 101–9, DOI: 10.1002/jmri.21987 (cited on p. 21).

[163] **Collins** Christopher M., Wanzhan Liu, Jinghua Wang, Rolf Gruetter, J. Thomas Vaughan, et al. "Temperature and SAR calculations for a human head within volume and surface coils at 64 and 300 MHz," *Journal of Magnetic Resonance Imaging* 19.5 (May 2004), 650–6, DOI: 10.1002/jmri.20041 (cited on p. 21).

[164] **Bodurka** Jerzy and Peter A. Bandettini. "Toward direct mapping of neuronal activity: mri detection of ultraweak, transient magnetic field changes," *Magnetic Resonance in Medicine* 47.6 (2002), 1052–8, ISSN: 1522-2594, DOI: 10.1002/mrm.10159 (cited on p. 22).

[165] **Atanasijevic** Tatjana, Maxim Shusteff, Peter Fam, and Alan Jasanoff. "Calcium-sensitive MRI contrast agents based on super paramagnetic iron oxide nanoparticles and calmodulin," *Proceedings of the National Academy of Sciences of the United States of America* 103.40 (Oct. 3, 2006), 14707–12, DOI: 10.1073/pnas.0606749103 (cited on p. 22).

[166] **Li** Wen-hong, Scott E. Fraser, and Thomas J. Meade. "A calcium-sensitive magnetic resonance imaging contrast agent," *Journal of the American Chemical Society* 121.6 (Feb. 17, 1999), 1413–4, DOI: 10.1021/ja9837021 (cited on p. 22).

[167] **Shapiro** Mikhail G., Tatjana Atanasijevic, Henryk Faas, Gil G. Westmeyer, and Alan Jasanoff. "Dynamic imaging with MRI contrast agents: quantitative considerations," *Magnetic Resonance Imaging* 24.4 (May 2006), 449–62, DOI: 10.1016/j.mri.2005.12.033 (cited on p. 22).

[168] **Friedland** Ari E., Timothy K. Lu, Xiao Wang, David Shi, George M. Church, and James J. Collins. "Synthetic gene networks that count," *Science* 324.5931 (May 29, 2009), 1199–202, DOI: 10.1126/science.1172005 (cited on p. 22).

[169] **Bonnet** Jerome, Peter Yin, Monica E. Ortiz, Pakpoom Subsoontorn, and Drew Endy. "Amplifying genetic logic gates," *Science* 340.6132 (May 3, 2013), 599–603, DOI: 10.1126/science.1232758 (cited on p. 22).

[170] **Kelman** Zvi and Mike O'Donnell. "DNA polymerase III holoenzyme: Structure and function of a chromosomal replicating machine," *Annual Review of Biochemistry* 64 (July 1995), 171–200, DOI: 10/cvmv32 (cited on pp. 22, 23).

[171] **Frank** Ekaterina G. and Roger Woodgate. "Increased catalytic activity and altered fidelity of human DNA polymerase ι in the presence of manganese," *The Journal of Biological Chemistry* 282.34 (Aug. 24, 2007), 24689–96, DOI: 10/cv5bmm (cited on p. 22).

[172] **Ochman** Howard and Allan C. Wilson. "Evolution in bacteria: evidence for a universal substitution rate in cellular genomes," English, *Journal of Molecular Evolution* 26.1-2 (1987), 74–86, ISSN: 0022-2844, DOI: 10.1007/BF02111283, URL: http://dx.doi.org/10.1007/BF02111283 (cited on p. 23).

[173] **Elowitz** Michael B. and Stanislas Leibler. "A synthetic oscillatory network of transcriptional regulators," *Nature* 6767 (2000), 335–338, DOI: 10.1038/35002125 (cited on p. 23).

[174] **Bernstein** Jacob G., Paul A Garrity, and Edward S. Boyden. "Optogenetics and thermogenetics: technologies for controlling the activity of targeted cells within intact neural circuits," *Current Opinion in Neurobiology* 22.1 (2012), 61 –71, ISSN: 0959-4388, DOI: http://dx.doi.org/10.1016/j.conb.2011.10.023 (cited on p. 23).

[175] **Jackson** Dean A., Ana Pombo, and Francisco Iborra. "The balance sheet for transcription: An analysis of nuclear RNA metabolism in mammalian cells," *The FASEB Journal* 14.2 (Feb. 2000), 242–54, URL: http://www.fasebj.org/content/14/2/242.long (cited on p. 23).

[176] **Zador** Anthony M., Joshua Dubnau, Hassana K. Oyibo, Huiqing Zhan, Gang Cao, and Ian D. Peikon. "Sequencing the connectome," *PLoS Biology* 10.10 (Oct. 23, 2012), e1001411, DOI: 10.1371/journal.pbio.1001411 (cited on p. 23).

[177] **Moosmann** Julian, Alexey Ershov, Venera Altapova, Tilo Baumbach, Maneeshi S. Prasad, et al. "X-ray phase-contrast *in vivo* microtomography probes new aspects of *Xenopus* gastrulation," *Nature* 497 (May 16, 2013), 374–7, DOI: 10.1038/nature12116 (cited on p. 24).

[178] **Issler** Sandy L. and Charlie C. Torardi. "Solid state chemistry and luminescence of X-ray phosphors," *Journal of Alloys and Compounds* 229.1 (Oct. 15, 1995), 54–65, DOI: 10/fpz8gt (cited on p. 24).

[179] **Larabell** Carolyn A. and Mark A. Le Gros. "X-ray tomography generates 3-D reconstructions of the yeast, *Saccharomyces cerevisiae*, at 60-nm resolution," *Molecular Biology of the Cell* 15.3 (Mar. 1, 2004), 957–62, DOI: 10/br3d8z (cited on p. 24).

[180] **Horowitz** Viva R., Benjamín J. Alemán, David J. Christle, Andrew N. Cleland, and David D. Awschalom. "Electron spin resonance of nitrogen-vacancy centers in optically trapped nanodiamonds," *Proceedings of the National Academy of Sciences of the United States of America* 109.34 (Aug. 21, 2012), 13493–7, DOI: 10.1073/pnas.1211311109 (cited on p. 24).

[181] **Dolde** Florian, Helmut Fedder, Marcus W. Doherty, Tobias Nöbauer, Florian Rempp, et al. "Electric-field sensing using single diamond spins," *Nature Physics* 7 (June 2011), 459–63, DOI: 10.1038/nphys1969 (cited on p. 24).

[182] **Hall** LT, GCG Beart, EA Thomas, DA Simpson, LP McGuinness, et al. "High spatial and temporal resolution wide-field imaging of neuron activity using quantum nv-diamond," *Scientific reports* 2 (2012), DOI: 10.1038/srep00401 (cited on p. 24).

[183] **Dean** Thomas, Biafra Ahanonu, Mainak Chowdhury, Anjali Datta, Andre Esteva, et al. "On the technology prospects and investment opportunities for scalable neuroscience," (2013), URL: http://www.stanford.edu/class/cs379c/course_projects_topics/report/ (cited on p. 24).

[184] **Filonov** Grigory S., Arie Krumholz, Jun Xia, Junjie Yao, Lihong V. Wang, and Vladislav V. Verkhusha. "Deep-tissue photoacoustic tomography of a genetically encoded near-infrared fluorescent probe," *Angewandte Chemie: International Edition* 51.6 (Feb. 6, 2012), 1448–51, DOI: 10.1002/anie.201107026 (cited on p. 24).